


Harmonic kicker cavity for high power operation

Gunn Tae Park, Jiquan Guo, Matthew Marchlik, Robert A. Rimmer,
Sarah Overstreet, and Haipeng Wang 

Accelerator Division, Jefferson Lab, Newport News, Virginia 23606, USA



(Received 26 March 2023; accepted 7 September 2023; published 21 September 2023)

A harmonic kicker cavity was originally proposed as an ultrafast bunch exchange device between energy recovery linac (ERL) and the circulator cooling ring (CCR) of the Jefferson Laboratory Electron-Ion Collider (JLEIC). The cavity is a transverse deflecting cavity that delivers a sharp kick synthesized using a linear combination of harmonic modes, which can be developed as a normal conducting quarter wave resonator (QWR). We present the development of the QWR as a high-power device (up to 7.5 kW) ready for a beam test: rf design (that involves the rf power optimization, tuning mechanism of five harmonic modes, power coupling), multipacting study, mechanical design with a water cooling system for high power operation, fabrication, and the rf bench tests.

DOI: [10.1103/PhysRevAccelBeams.26.091002](https://doi.org/10.1103/PhysRevAccelBeams.26.091002)

I. INTRODUCTION

A harmonic kicker cavity was proposed as an ultrafast electron bunch exchange device in the context of the circulator cooling ring (CCR) development as a part of the JLEIC cooling system R&D [1,2]. In the CCR (for a schematic overview of the CCR and the beam parameters, see Fig. 1(a) and Table I, respectively), the recirculating electron bunches at bunch frequency of 476.3 MHz are replenished in a way that the “exchanged” bunches at the frequency of 43.3 MHz (the frequency was planned to eventually increase to 86.6 MHz in a possible luminosity upgrade of the JLEIC where the rf system and the bunch frequency would change to 952.6 MHz) are deflected into/out of the ring by a pair of rf kickers, as shown at the second to top in Fig. 1(a). In order for this kick to not disturb the beam dynamics of the neighboring bunches (circulating the ring), the kick was synthesized from a linear combination of five (odd) harmonic modes with a fundamental frequency of 86.6 MHz—this frequency is compatible with the exchange frequency of both 43.3 and 86.6 MHz—so that its temporal profile [shown at the bottom in Fig. 1(a)] is sharply peaked around the exchanged bunches only and rapidly falls down to near zero elsewhere. More details on the design principle of a harmonic kicker and its role in the CCR beam dynamics are discussed in [3].

A QWR with its coaxial geometry (see Fig. 1(b), where a cross section of the QWR is shown) can naturally

accommodate the five (odd) harmonic modes as its resonant modes in a reasonably compact size, half of the double quarter wave resonator (DQWR), for example. In Fig. 1(b) that the tip of the inner conductor is configured so that the electromagnetic fields in the gap (between the tip and the bottom) provide a vertically deflecting kick to the beam. As per Table I, for a beam with energy of 55 MeV, a kick voltage of 25 kV for each mode is needed for 2.5 mrad deflection. The total kick voltage of 125 kV can be achieved straightforwardly by an optimally designed normal conducting QWR with about 7.1 kW total rf power, which is some advantage over a stripline cavity that can also provide a sharp kick with traveling waves [4]. On the other hand, vertical asymmetry of the QWR gives rise to the significant multipole fields that could degrade beam dynamics and needs a scheme that suppresses the effects (for a multipole cancellation scheme, see [5,6]). The five harmonic modes from the rf source are nearly critically coupled into the cavity via a single loop input power coupler, located near the top utilizing a dominant inductive coupling. The tuning of the resonant frequencies of the cavity is achieved by a five-plunger tuner system, where five stubs along the outer conductor of the cavity are inserted into the cavity with the frequency tuning determined by the insertion depths.

The first prototype of a QWR kicker cavity was successfully developed with the fundamental frequency of 95.2 MHz [1,2], which was compatible with the first version of beam parameters of the CCR—the beam parameters of the CCR and a harmonic kicker went through a couple of revisions before settled down to the current values as listed in Table I. The prototype was mostly based on the rf design not intended for high-power operation nor the beam test and was used only as proof-of-principle for the feasibility of the QWR as a harmonic kicker. In this

Published by the American Physical Society under the terms of the Creative Commons Attribution 4.0 International license. Further distribution of this work must maintain attribution to the author(s) and the published article's title, journal citation, and DOI.

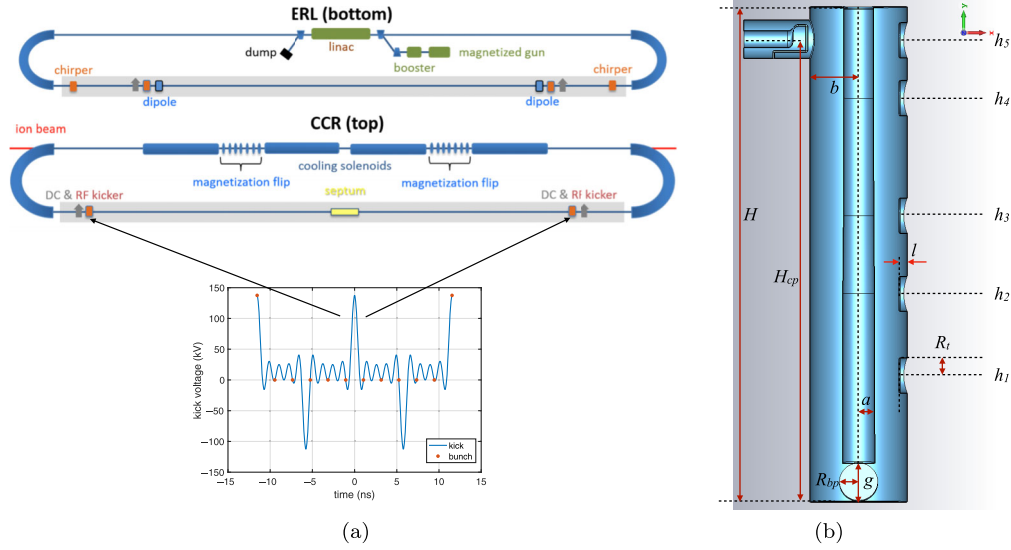


FIG. 1. The schematic overview of the CCR and the QWR model. (a) The overview of the CCR with a harmonic kicker system, denoted as RF kickers. A temporal profile of a harmonic kick is shown at the bottom. (b) The cross-sectional view of the QWR.

paper, the development of the second prototype with a fundamental frequency of 86.6 MHz (for the design development, see [6,7]) is presented in some detail. The second prototype is an upgraded version for a high power operation (~ 7.5 kW) in beam test (which requires a vacuum-tight device up $\sim 10^{-9}$ mbar). A high-power, high vacuum operation requires power optimization, rf breakdown and multipacting investigation, nearly critical rf couplings (between 0.5 and 2), and multiphysics analysis that assesses the effects of the rf heating and evacuation of the cavity. Moreover, the heating requires an effective cooling system. A high power operation makes maintaining a stable kick profile in Fig. 1(a) particularly challenging. A high-power operation involves relatively high temperatures and large temperature drifts even under the cooling scheme,

leading to significant resonant frequency shifts via thermal expansion/contraction of the cavity wall. For a stable kick profile, each harmonic mode from the rf source at drive (which is nominal) frequency must couple into the cavity with the nominal amplitude/phase as prescribed in Table I. With the amplitude of each mode modulated upon coupling depending on the deviation of the resonant frequency from the drive frequency, the resonant frequency shifts by thermal drifts must be compensated by a tuning system. This requirement, combined with possible bunch frequency change (for flexible beam operation) and the compensation of another resonant frequency deviations from fabrication/installation of the cavity, demands an effective tuning system with a large tuning range of $\delta f/f \sim \pm 4 \times 10^{-4}$ for each mode and relatively fast in action. The impedance

TABLE I. The Beam and kicker parameters of the CCR. The Twiss parameters are at the kickers. The numbers after \pm signs are the voltage tolerances for the beam quality control [3].

Parameters (CCR)	Unit	Value	Modes	Parameters (kicker)	Unit	Value
Beam energy E_e	MeV	55	86.6 MHz	Kick voltage V_1	kV	-25 ± 0.38
Kick angle θ	mrad	2.5	259.8 MHz	Kick voltage V_2	kV	-25 ± 0.38
Turns \mathcal{N}		11	433 MHz	Kick voltage V_3	kV	-25 ± 0.38
Kick frequency f_k	MHz	86.6	606.2 MHz	Kick voltage V_4	kV	-25 ± 0.38
Bunch frequency f_b	MHz	476.3	779.4 MHz	Kick voltage V_5	kV	-25 ± 0.38
Bunch charge Q_b	nC	1.6				
Bunch length l_b	cm	3				
Energy spread δE		3×10^{-4}				
Emittance e^n	mm-mrad	36				
Twiss parameter α		0				
Twiss parameter β	m	120				

study with a high-intensity beam current will be discussed in a separate publication.

A prototype cavity for high vacuum, high power operation was fabricated and tested with a beam at the Upgraded Injector Test Facility (UITF) of the Jefferson Lab (for a detailed description of the test and its preparation, see [8]). The test was done successfully at the beam energy of 9 MeV, and the rf power of the kicker cavity was accordingly scaled down to about 150 W for the test. An application of a harmonic kicker can possibly be extended beyond the CCR/JLEIC beam exchange to a more general context of the beams with a wide range of time structures and deflecting angles. The successful prototyping of the current kicker cavity will render much confidence and lessons in developing many other (high power in particular) kicker systems to come in the future.

II. ANALYTICAL MODEL FOR QUARTER WAVE RESONATOR (QWR)

Before performing numerical rf simulations that would determine a highly optimized geometry, we analytically study the performance of the QWR based on a simple semiclosed coaxial structure model, which would give a rough estimate for the geometrical parameters of the cavity as well as a better understanding of the underlying mechanism of the cavity performance. The QWR cavity is designed to have five odd harmonics of the fundamental frequency of $f_1 = 86.6$ MHz and deliver the kick voltage of $V_k = 25$ kV in each harmonic mode. To control the beam loss up to $\pm 6\sigma$ (where $\sigma = 5.9$ mm is rms value of the transverse beam size determined in beam dynamics simulations [9]), the gap size g and beam pipe aperture $2R_{bp}$ are constrained to be $g = 2R_{bp} = 0.07$ m. In Fig. 1(b), the height h of the QWR is roughly given as $h = \lambda_1/4 = 0.866$ m, where $\lambda_1 = 3.46$ m is a wavelength corresponding to the fundamental frequency. Higher modes naturally exist as odd harmonics for the same given height. For optimal kick efficiency, all the harmonic fields in the cavity are on-crest (i.e., with rf phase $\phi = 0$) when the electron bunch passes the cavity center. Then ‘‘synchronization condition’’ that maximizes the transit time factor with respect to the ninth harmonic frequency f_9 (with the shortest wavelength λ_9) sets the outer conductor radius b to satisfy $2b/c = 1/(2f_9)$, i.e., $b = 92.6$ mm, where c is the speed of light. But the synchronization condition is based on the constant kick profile and the value of b is expected to be flexible for realistic profiles. Finally, a is determined to minimize the total power loss P_d on the copper wall of the cavity, which is given as

$$P_d = \sum_{n=1}^5 \frac{V_{k,n}^2}{R_{\perp,n}}, \quad (1)$$

where $V_{k,n}$, $R_{\perp,n}$ are kick voltage and transverse shunt impedance of n th odd harmonic mode, respectively. Based

on the simple geometry, an analytical formula for the transverse shunt resistance R_{\perp} is available [2] as

$$R_{\perp,n} = \frac{128\pi f_1 (b\xi)^2 Z_0^2 F_n^2 T_n^2}{cg^2 R_{s,n}} \left\{ \frac{1}{b\xi} + \frac{1}{b} + \frac{8f_1}{c} \ln \frac{1}{\xi} \right\}^{-1}, \quad (2)$$

$$\text{where } R_{s,n} = \sqrt{\frac{\pi f_n \mu_0}{\sigma_0}}, \quad Z_0 = \frac{\eta_0}{2\pi} \ln \left(\frac{1}{\xi} \right). \quad (3)$$

In (2), ξ is the ratio a/b , $R_{s,n}$ is the surface resistance associated with n th odd harmonic mode ($\mu_0 = 4\pi \times 10^{-7}$ N/A² is vacuum permeability and $\sigma_0 = 5.8 \times 10^7$ S/m is ideal conductivity of pure copper at room temperature), Z_0 is the characteristic impedance of transmission line (the QWR) with vacuum wavelength impedance $\eta_0 = 120\pi \Omega$, F_n is a fringe field factor, and T_n is a transit time factor of the n th odd harmonic mode, respectively. A fringe factor F_n is defined as

$$F_n = \frac{1}{2a\mathcal{E}_n} \int_{-b}^b dz \{ E_{\perp n}(z) - cB_{\perp n}(z) \} \\ = \frac{1}{2a\mathcal{E}_n} \int_{-b}^b dz E_{\perp n}(z). \quad (4)$$

Here $E_{\perp n}$, $B_{\perp n}$ are vertical electric fields and horizontal magnetic fields on the beam axis, respectively. The \mathcal{E}_n is a vertical electric field on a beam axis assumed to be uniform over the gap. Thus the shunt voltage $V_{\perp n}$ of n th harmonic across the gap is given as $V_{\perp n} = g\mathcal{E}_n = gE_{\perp}(z=0)$. The last equality in (4) holds because $B_{\perp n}$'s are all antisymmetric along the beam axis according to the CST-MWS simulation. A transit time factor T_n is defined as

$$T_n = \frac{1}{2a\mathcal{E}_n F_n} \int_{-b}^b dz \left\{ E_{\perp n}(z) \cos\left(\frac{2\pi f_n z}{c}\right) - cB_{\perp n}(z) \sin\left(\frac{2\pi f_n z}{c}\right) \right\}. \quad (5)$$

F_n 's and T_n 's are the functions of a , b , and g , which can be fitted via a two-variable nonlinear regression with a series of parameter scanning (with respect to ξ and b) in the simulations (see Table VIII in Appendix A for the explicit fitting results). Then the power P_d in (1) is obtained as a function of a and b via F_n and T_n : By inserting (4), (5) (in Appendix A) into (2) and subsequently (1). The total power (1) as a function of a and b is plotted in Fig. 2. According to Fig. 2, the bigger b would imply the smaller minimum power loss at bigger ξ . For example, if $b = 88$ mm is selected, the power loss will be the minimum $P_{\text{tot}} = 5$ kW at $\xi = 0.36$, i.e., $a = 31.7$ mm.

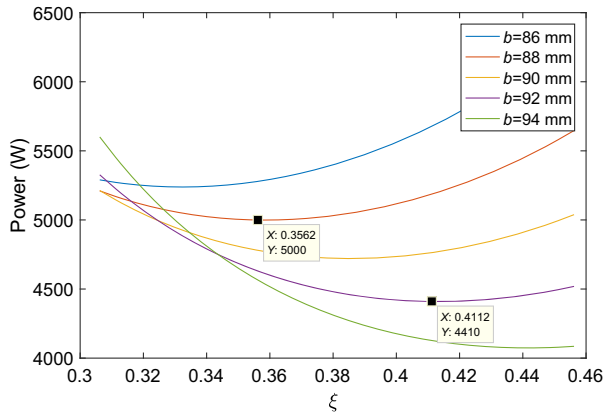


FIG. 2. The analytical evaluation of power as a function of b and ξ .

III. ELECTROMAGNETIC DESIGN OF THE HARMONIC KICKER

A. Power optimization

Unlike the first prototype [2], the second prototype has an even larger beam pipe size, which makes deviation from the analytical description significant. For more accurate optimization for the minimum power loss, a series of numerical simulations using a 3D FEA code CST-MWS [10] was necessary. Using analytically determined optimal dimension for the cavity geometry from the previous section as a starting model, a two-parameter scanning of a and b was done (The actual sweep was with $\xi = a/b$ instead of a). The resulting power distribution over the swept parameters is shown in Fig. 3. In Fig. 3, the power tends to get lower as b and ξ increase but TE₁₁ mode

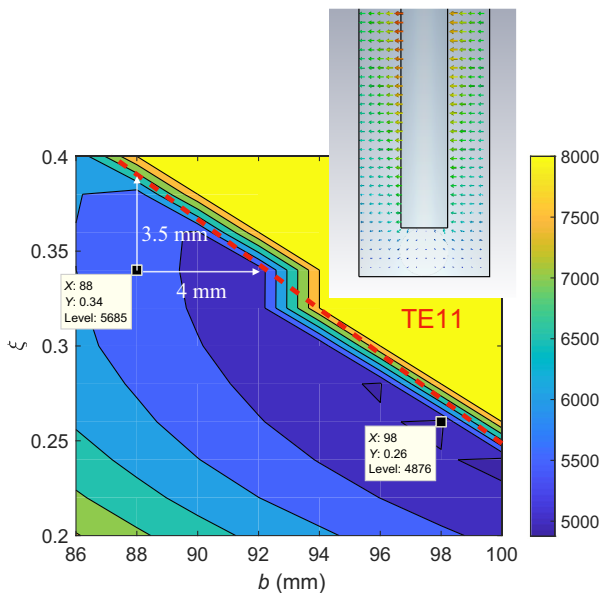


FIG. 3. Power optimization with the constraints. The TE₁₁ modes show up in the yellow area above the threshold.

(shown in Fig. 3) starts to develop as the fifth mode in frequency spectrum as $a + b$ value exceeds a certain threshold. As a result, the region of lower power loss available to the harmonic kicker cavity corresponds to the proximity (the dark blue region in Fig. 3) of the threshold boundary beyond which the TE modes develop. Although the global minimum power of 4.9 kW is obtained with $b = 98$ mm, $\xi = 0.26$, this would lead to a too-small inner conductor in diameter, which might interfere with the cooling channel installation into the inner conductor. Alternative choice was made at $b = 88$ mm $\xi = 0.34$ ($a = 30$ mm), where the dissipated power is $P_{\text{diss}} = 5.7$ kW for the required kick voltage. This compares with the analytical estimation in Sec. II, which is based on a coaxial structure without beam pipe and smaller by about ~ 700 W. The choice of the dimensions takes into account an engineering margin of 3–4 mm to the threshold boundary. The influence on the power of blending to various corners is minimal except for the tip of the inner conductor, which was set to the minimum accordingly. Although the larger blending on the tip decreases the peak electric field, it also decreases transverse shunt impedance, which implies more energy in the cavity needed for the given target kick voltage, leading to significant increases in power.

B. Rf break down study

For a full power operation, the Kilpatrick limit for the rf breakdown was checked for the kicker cavity. The Kilpatrick limit for each harmonic mode was numerically estimated as illustrated in Fig. 4(a) and listed in Table II. The peak surface field for each mode as scaled to the target kick voltage was obtained from the simulation. The comparison was done mode by mode and listed in Table II, which shows the peak surface fields are significantly lower than the Kilpatrick limit for every mode. The phase of each mode is set to zero so that all the modes add up constructively to define a total field on the moment a kicked bunch passes through the kicker center. Moreover, with the peak fields of the five modes all located at the tip of the inner conductor, the maximum possible surface peak field (of a total field) then would be a sum of the last column in Table II, i.e., 13.6 MV/m. A more realistic estimation of the total peak field is somewhat more ambiguous. The superposition of 3D field maps of five modes in the CST simulation shows the total peak field to be 7.8 MV/m, because the peak field location of each mode is slightly different. We conclude the actual total peak field will be between 7.8 MV/m and 13.6 MV/m. With the Kilpatrick limit [see the defining equation in Fig. 4(a)] applicable only with a single frequency mode, we find an “effective” single frequency mode that the total field in a short time period of our interest, i.e., during a time window of ± 0.2 ns when a bunch goes through the cavity and the total surface peak field comes close to the predicted maximum

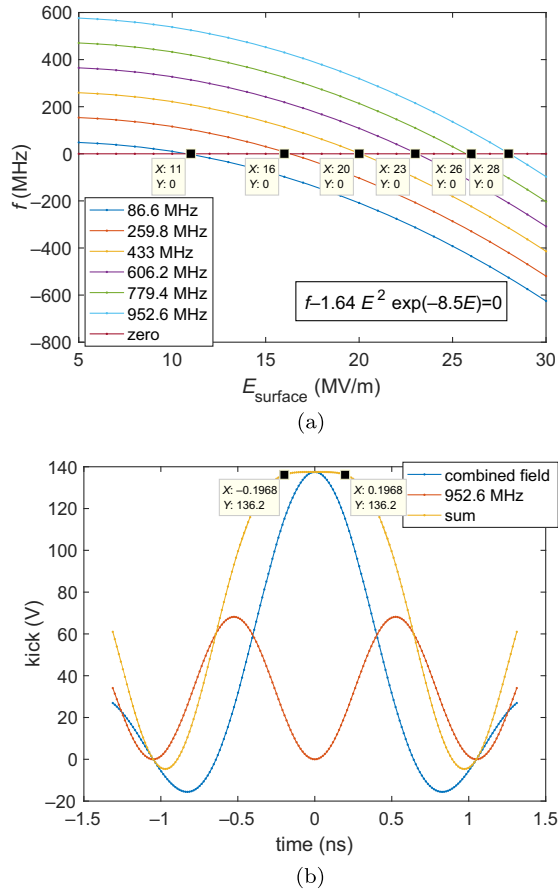


FIG. 4. Kilpatrick limit for the harmonic kicker. (a) Kilpatrick limit: the limiting fields were obtained as a graphical solution of the Kilpatrick equation shown above. The curves refer to lhs of the equation. (b) A combined harmonic kick is compensated by a single frequency kick at 952.6 MHz, which implies the total fields can be approximated by this single frequency mode.

7.8–13.6 MV/m. In Fig. 4(b), one can see the temporal profile of the total field would be flattened by a hypothetical 952.6 MHz mode over the time window of ± 0.2 ns. This suggests that during bunch passage the total field can be effectively considered as a single frequency mode at ~ 952.6 MHz. The Kilpatrick limit of 952.6 MHz mode

TABLE II. Kilpatrick limit for the harmonic kicker. E_K is the Kilpatrick limit and E_{pk} is a normalized surface peak field of the kicker cavity.

Modes	f	E_K	E_{pk}
Units	MHz	MV/m	MV/m
1	86.6	11	2.7
3	259.8	16	2.9
5	433	20	2.8
7	606.2	23	2.7
9	779.4	26	2.5
Total	952.6	28	7.6–13.6

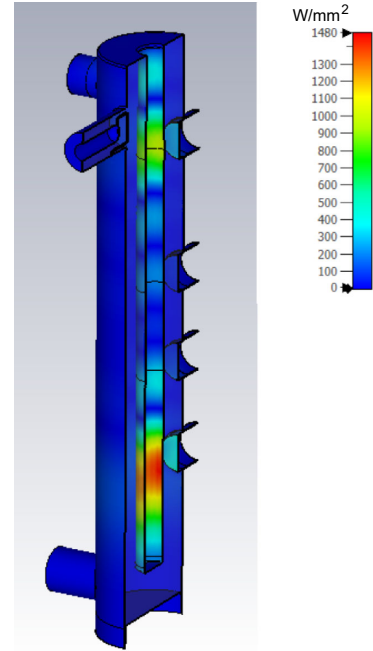


FIG. 5. The modified Poynting vector.

is again numerically solved to be about 28 MV/m [see Fig. 4(a)], well above the possible range of the total peak surface fields.

In addition to the analysis based on the peak surface electric field, the pulsed surface heating temperature and the modified surface Poynting vector (S_c) were evaluated and compared to the threshold values for the breakdown [11]. The modified Poynting vector is defined as $S_c = \Re[S] + \Im[S]/6$ for the given complex Poynting vector $S = \vec{E} \times \vec{H}$. The computed maximum modified Poynting vector in the cavity is only 1450 W/mm² (Fig. 5), which is much less than the scaled threshold 10.6×10^6 W/mm² to a pulse length of 2.2 ns (see the bottom figure of Fig. 1(a) for the pulse length of a harmonic kicker). The threshold scales with the pulse length t_p as $\propto t_p^{-1/6}$ from 5×10^6 W/mm² for a 200 ns pulse length as reported in [11,12] in the context of a traveling wave structure. The peak heating temperature [see Fig. 18(c)] at the maximum modified Poynting vector location is also only around 60 °C, whose temperature rise from the room temperature is about the same as the threshold temperature rise of 40 °C for the oxygen-free copper (OFC) [13].

C. Harmonic frequency adjustment and tuner design

After power optimization, the resonant frequencies were tuned to the nominal harmonic frequencies by adjusting the height of the cavity (for rough tuning) and tapering the inner conductor in multiple segments (for fine-tuning). Additional tuning by a set of five stub tuners [See Fig. 1(b)]

is to compensate for any frequency deviations (from the nominal frequency) due to fabrication errors, temperature drifts, beam dynamics requirement, and small microphonics during the operation. In particular, possible bunch frequency change $f_b \sim 476.3 \text{ MHz} \pm 67 \text{ kHz}$ (from the CCR beam dynamics requirement for possible path length change) and temperature drifts from the imbalance between the rf heating and cooling system would require cavity frequency adjustment in the range of $\delta f/f \sim \pm 1.4 \times 10^{-4}$ and $\delta f/f \sim \pm 0.8 \times 10^{-4}$, respectively—the tuning range for temperature drift was estimated from $\delta f/f \sim \delta l/l \sim \kappa \delta T$ (with $\kappa = 16 \times 10^{-6} \text{ K}^{-1}$ being a thermal expansion coefficient of a copper) for the temperature drift of $\delta T \sim \pm 5 \text{ K}$. This will make the tuning range of $\delta f/f \sim \pm 4 \times 10^{-4}$ appropriate for a combination of the two dominant factors.

First the rough tuning was done by adjusting the height, whose fractional frequency response ($\delta f/f$) is linear with the common slope of $1.15 \times 10^{-3} \text{ mm}^{-1}$ for all modes. This is consistent with Slater’s cavity perturbation theorem, i.e., $\delta f/f \sim \delta l/l$ (with $l = 0.83 \text{ m}$), which is valid in small perturbation. A rough tuning achieved the frequency deviations of $\Delta f/f \leq \pm 2.5 \times 10^{-3}$ for all modes at the height $h = 903 \text{ mm}$. Before fine-tuning (by tapering), the stub tuner configuration was determined to secure the tuning range. A harmonic frequency response to any small change in cavity geometry would be described by Slater’s cavity perturbation theorem, i.e., the frequency response of each harmonic mode to the small cavity energy change is given as

$$\Delta f_i = f_i \Delta U_i, \quad \text{where } U_i = \int_V dV \{ \epsilon_0 E_i^2 - \mu_0 H_i^2 \}. \quad (6)$$

Here f_i , U_i , E_i , H_i are the frequency, the stored energy, and the electric and magnetic field of the i th odd harmonic, respectively, while V is the cavity volume. Tuning is done by changing U_i ’s with a set of independent “tuning points” h_j ’s (with $j = 1, \dots, M$ for M tuning points), i.e., $\Delta U_i = \sum_{j=1}^M (\partial U_i / \partial h_j) \Delta h_j$, which leads to

$$\Delta f_i = T_{ij} \Delta h_j, \quad \text{where } T_{ij} = \frac{\partial f_i}{\partial h_j} = f_i \frac{\partial U_i}{\partial h_j}. \quad (7)$$

Here T is called a tuning matrix. The (i, j) element of T corresponds to the first order frequency response of i th odd harmonic to the change in j th tuning point. For the given five modes, five tuning points would make (7) a 5×5 matrix equation that can be critically determined and always be solved for Δh ’s simply by inverting T .

Now arbitrary h_j ’s can be specified to a particular tuning mechanism. For stub insertion adjustment, h_j is an insertion depth of the j th stub. For small changes of Δh_j we have

$$T_{ij} = f_i \int_{S_j} da \{ \epsilon_0 E_i^2 - \mu_0 H_i^2 \}, \quad (8)$$

where S_j is the cross-section area of the j th stub. In terms of physical quantities, T in (8) is approximately the surface integral of “frequency sensitivity density”, which is a function of area element via electric and magnetic field profiles on the area. Thus the broad tuning range can be found using an extensive scanning of a set of tuning parameters in the simulation with a high mesh setting (tetrahedral meshing $> 5 \times 10^5$ with the curved element of order 2): the vertical position, insertion depth (into the cavity), radius and corner blending of each stub. In particular, the vertical positions were determined in Fig. 6(a) so that all the tuning matrix elements [see (10)] are reasonably large enough for a small stub motion. Some of the determined positions (three in the middle) were shared with the tapering points, which require shallow tapering angles. The stubs were inserted into the default position in the cavity for bidirectional tuning. A deep insertion, in spite of a higher tuning range with stronger fields, would lead to more heating and a wider frequency deviation spectrum with nonlinear frequency sensitivity as shown in 6(b). Therefore the (default) insertion depths of the stubs are determined to be 15 mm into the cavity

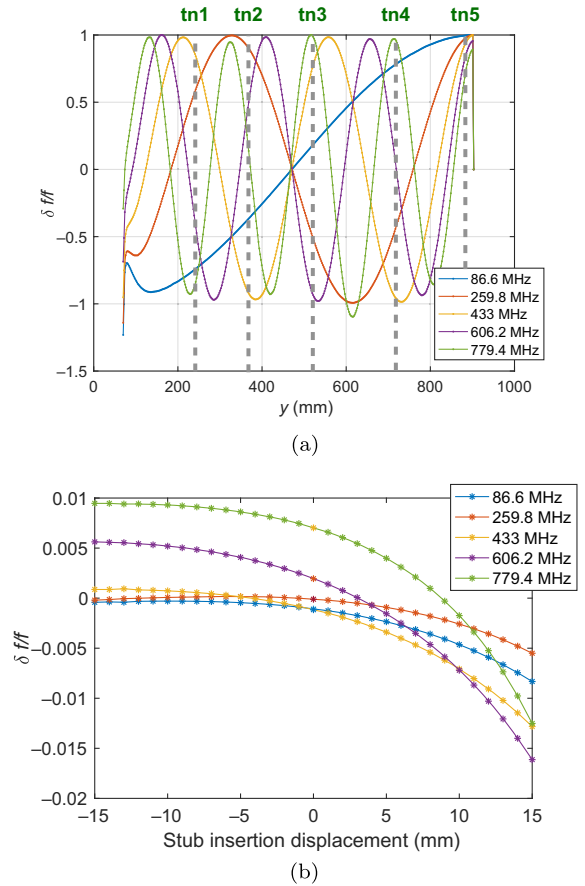


FIG. 6. Frequency adjustments. (a) The vertical location of the tuning points based on frequency sensitivity density. The density is normalized to 1. (b) The $\delta f/f$ for each mode as the stubs are inserted. The frequency response is not linear.

volume, balancing frequency spectrum control and a large tuning range—this naturally sets the motion range of the stubs to be ± 15 mm. For a larger tuning range, each stub with a larger cross section and a sharper blending to the edge is inserted as demonstrated. The sharper blending enhances the field strength and increases the tuning range. To compensate for the overall frequency change during the insertion to default position, a few iterations between rough tuning and stub configuration adjustments are needed before reaching the final height $h = 899.5$ mm, with which the fifth mode reaches target frequency at the insertion depth of 15 mm.

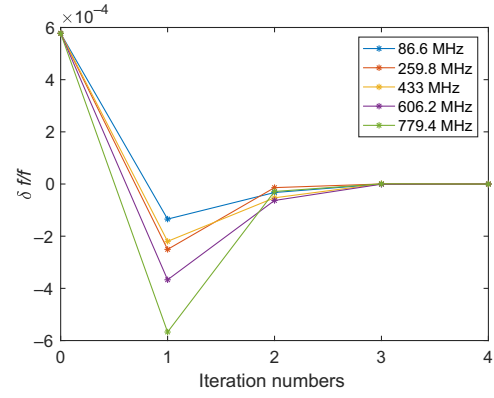
With the stub tuners inserted, a finer tuning by tapering the inner conductor on five locations for five modes was done to achieve the resolution of $\delta f_i/f < 3 \times 10^{-5}$ for all i 's, which is required to maintain a temporal kick field profile and the rf power loss under control. In practice, \mathcal{T} is evaluated by parameter scanning (sweeping Δh_j 's while tracking Δf_i 's) in CST-MWS simulations and applying a linear fit to the outputs (see Appendix B for details of fitting). The optimal tuning matrices, \mathcal{T}_t for inner conductor tapering and \mathcal{T}_s for the stub insertion, are obtained (in units of MHz/mm) as

$$\mathcal{T}_t = \begin{bmatrix} -0.530 & -0.344 & 0.142 & 0.446 & 0.263 \\ -0.509 & 1.216 & -0.863 & -0.516 & 0.609 \\ -0.056 & -0.638 & 0.982 & -1.003 & 0.581 \\ -0.295 & 0.530 & -0.513 & -0.236 & 0.283 \\ -0.241 & -0.262 & 0.267 & -0.093 & 0.030 \end{bmatrix}, \quad (9)$$

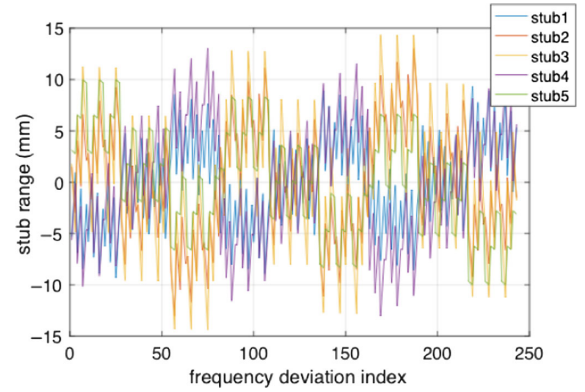
$$\mathcal{T}_s = \begin{bmatrix} -0.019 & -0.012 & -0.003 & 0.008 & 0.011 \\ 0.005 & 0.025 & -0.043 & -0.034 & 0.021 \\ 0.047 & -0.114 & 0.032 & -0.116 & 0.003 \\ -0.068 & 0.035 & -0.159 & -0.094 & -0.045 \\ -0.226 & -0.099 & 0.076 & 0.029 & -0.121 \end{bmatrix}. \quad (10)$$

Once \mathcal{T} is known, frequency deviations can be compensated by solving for Δh_j 's in (7). With \mathcal{T}_t in (9), Δh_j 's determine the tapering slopes on the inner conductor. With \mathcal{T}_s in (10), Δh_j 's are the insertion depth of the stubs. Because the actual frequency response of each mode is not fully linear, the tuning based on the tuning matrices fails to tune the frequencies exactly, which requires some iterations of tuning based on (7) for a desired tuning accuracy of $\delta f/f \sim \pm 3 \times 10^{-5}$, as demonstrated in Fig. 7(a).

The tuning range of the stub tuners can be approximately estimated based on the linear matrix \mathcal{T}_s in (10) and is illustrated in Fig. 7(b). In Fig. 7(b), the horizontal axis is a distribution of the instances of fractional frequency



(a)



(b)

FIG. 7. The tuning range of the stubs based on a linear response. (a) The iteration process for frequency tuning, starting with the frequency deviation of $\delta f/f = 5.7 \times 10^{-4}$. (b) The tuning range of the stubs.

deviations of the cavity in the range of $\delta f/f \sim \pm 6 \times 10^{-4}$. Here an instance (a point on the horizontal axis) is a quintuplet whose entry corresponds to the fractional frequency deviation for each harmonic mode, i.e., $(\delta f_1/f_1, \delta f_2/f_2, \delta f_3/f_3, \delta f_4/f_4, \delta f_5/f_5)$. Each instance is labeled as “frequency deviation index”—we used 250 different instances in the distribution. The vertical axis refers to the distance traveled by each stub to tune the frequency back to the target for a given instance of frequency deviation, using the Slater cavity perturbation theorem with (10). Five stubs define five curves (with different colors) for the distribution. Given that the traveled distances must be all within ± 15 mm, which is the mechanical upper/lower limit of the stub motion, some of the curves in Fig. 7(b) nearly touching the ± 15 mm limit suggest $\delta f/f \sim \pm 6 \times 10^{-4}$ is the maximum tuning range. Given a rather long travel distance of the stubs, the Slater cavity perturbation theorem has limitations and a more accurate tuning range evaluation requires a different approach that takes into account a nonlinear response to the stub insertion. In Appendix C, we scanned the frequency response over a full range of stub motion, obtaining

a nonlinear fit. The tuning range plot using the nonlinear fit curves (but still using the iteration based on a linear matrix) is shown in Fig. 30(f).

D. Coupler design

A single loop power coupler was designed to couple five harmonic modes into the kicker cavity. For each mode, the generator power P_g needed to maintain a constant kick voltage within the cavity is determined by the rf coupling β 's. The baseline design of rf coupling to the cavity is based on a negligible beam loading case with a low kick voltage of 125 kV (see Table I). Then the approximate formula for the generator power on resonance is given as

$$\begin{aligned} P_{g,\text{tot}}^0 &= \sum_{n=1}^5 P_{g,n} = \sum_{n=1}^5 \frac{V_n^2 (1 + \beta_n)^2}{R_n 4\beta_n} \\ &= \sum_{n=1}^5 P_{\text{wall},n} \frac{(1 + \beta_n)^2}{4\beta_n}, \end{aligned} \quad (11)$$

where V_n , R_n , β_n , $P_{\text{wall},n}$ are the kick voltage, shunt impedance, rf coupling coefficients, and wall loss of the n th mode, respectively. The rf coupling is defined as $\beta_n = Q_{0,n}/Q_{e,n}$ with $Q_{0,n}$ and $Q_{e,n}$ being unloaded and external quality factor for n th mode. With a single loop coupler configuration, exact critical couplings for all five modes cannot be achieved and only the acceptable range of the (near critical) couplings (for the minimum power) was considered. In Fig. 8(a), the power increase due to the small deviation of β from critical coupling is not big, and even a relatively large deviation is allowed in case of overcoupling. It is advantageous for the minimum total power to have higher frequency modes closer to the critical coupling because they have smaller shunt impedances and require more power. The estimation based on (11) gives the target range of all the β_n 's in $0.7 < \beta < 1.5$ to keep the additional total generator power (due to rf coupling) below 300 W.

For the rf coupling in the cavity, a loop coupler is placed near the top plate where the inductive coupling via magnetic field is dominant. The detailed geometrical configuration of the loop antenna was determined with the extensive use of CST-MWS code [10] utilizing geometrical parameter scanning capability while tracking β 's and is shown in Fig. 8(b). The characteristic impedance of the coupler is matched to 50Ω of the standard transmission line. Given the broadband (80–800 MHz) nature of the coupling, a more sophisticated configuration than a single frequency coupling is required: a loop with its tip grounded gives far better control over the convergence of the β 's for the five harmonic modes (i.e., β values for all the modes are close to one another). The grounded loop couples to the fields via both electric and magnetic fields. The straight section of the grounding L-leg mostly picks up the electric

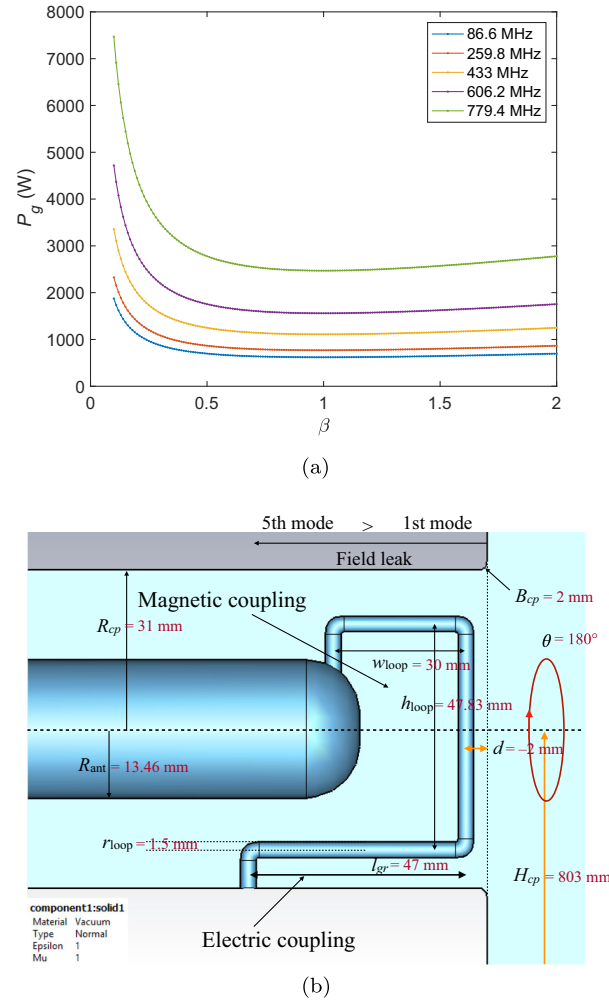


FIG. 8. The coupler design and power expectation. (a) The source power vs β for each mode. (b) The geometry of loop coupler.

field (proportional to its length), while the area enclosed by the loop picks up magnetic fields. Moreover, because of the geometrical location of the leg and the loop area, different modes are selectively coupled, i.e., lower modes that cannot penetrate deep into the coupler port has mostly magnetic coupling, while the higher modes with deeper penetration have both couplings. The balance between these two contributions for each mode was achieved by extensive parameter scanning of the vertical position of the coupler port and insertion depth. The remaining geometrical parameters [as shown in Fig. 8(b)] were also scanned for finer tuning of the coupling. Finally, the loop geometry was further tuned so that the couplings and the corresponding power are insensitive to the deviation from the ideal configuration. The tip is anchored on a rotatable flange so that some coupling adjustment is available via rotating the loop before the final installation.

Now we remark on some technical aspects of the coupling simulations. The rf coupling β for each harmonic

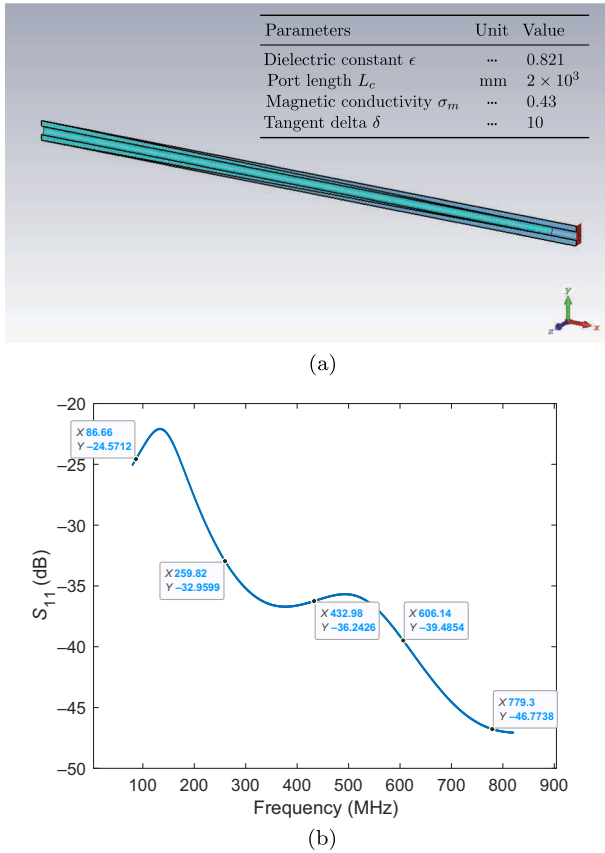


FIG. 9. The optimization of an absorber. (a) The geometry of the heat load. The lighter blue is the heat absorber. The red plane is a waveguide through which input power leaks in. (b) The optimized S_{11} parameter of the heat load.

mode was obtained, via the evaluation of quality factors Q_0 and Q_e , in 3D simulations using CST-MWS. Although there exists in CST-MWS a simple way to evaluate Q_e based on a waveguide port set up at the end of the coupler port, this involves a rather cumbersome boundary matching to properly account for incoming and outgoing rf fields through the coupler port [14,15]. Instead, we use a different method developed in [16] that utilizes a perfect absorber of

the rf fields. A perfectly absorbing load placed at the end of the coupler port would make electromagnetic fields a purely outgoing traveling wave through the coupler port (without reflecting back into the cavity). Then the heat loss at the load by the outgoing waves would account Q_e accurately.

First, the specification of an artificial, perfect absorber was determined by the optimization simulation in frequency domain solver targeting the lowest reflection for all the harmonic modes. An artificial absorber shown in Fig. 9(a) is an elongated (2 m long) tapered cone for minimum reflection. The optimized material properties are also shown in Fig. 9(a). In Fig. 9(b), S_{11} parameters obtained in the simulations are shown to be small (< -25 dBm) for all the harmonic modes (ranging from 86 to 800 MHz).

With the absorber integrated into the cavity model through the coupler port, the rf power coupling evaluation was done in eigensolver of CST-MWS: the coupling constant $\beta = Q_0/Q_e$ for each mode and the corresponding total source power P_g according to (11). With a lossy material present in the simulation, the conventional quality factor Q_{pert} computed in CST accounts for both the surface loss (of the cavity) and the volume loss (of the absorber), corresponding to the loaded quality factor Q_L . On the other hand, Q_{lossy} accounting for the volume loss of the absorber only corresponds to Q_e , from which Q_0 can be determined as $Q_0 = Q_e Q_L / (Q_e - Q_L)$. This evaluation can be compared with the direct evaluation of the Q_e , based on the loaded frequency with a waveguide port setup, which is listed in Table III. Except for the fundamental frequency mode, the evaluations for all the higher modes agree very closely. In order to account for some heating (especially in high power operation) leading to decrease in Q_0 in the real cavity, the coupling was slightly over-coupled and the conductivity of the copper was slightly lowered to $\sigma_c = 4.8 \times 10^7$ S/m $< \sigma_0 = 5.8 \times 10^7$ S/m (σ_0 is ideal conductivity of copper at room temperature).

The parameter scanning results are summarized in Fig. 10. All the relevant geometrical parameters of the

TABLE III. The figures of merit [including $Q_e(f_i)$] for harmonic modes as evaluated through the waveguide port method with a loaded frequency. Q_e is the external quality factor with an absorber. In evaluation, realistic conductivity for copper $\sigma = 4.8 \times 10^7$ was used. The bandwidth is computed as $\Delta_{\pm 3dB,n} = \pm f_n / 2Q_{L,n}$.

Modes	f	Q_0	R_{\perp}	Q_e	$Q_e(f_i)$	β_{op}	$\Delta_{\pm 3dB}$	P_d	P_g	R_{\perp}/Q_0	G
Units	MHz	$\times 10^4$	M Ω	$\times 10^4$	$\times 10^4$		kHz	kW	kW	Ω	Ω
1	86.6	0.57	1.38	0.78	0.85	0.74	± 13.1	0.472	0.47	241	15
2	259.8	0.98	0.71	0.83	0.84	1.21	± 28.9	0.832	0.88	76	43
3	433	1.28	0.53	1.07	1.09	1.22	± 37.1	1.189	1.20	41	77
4	606.2	1.51	0.37	1.29	1.29	1.20	± 43.6	1.683	1.69	25	107
5	779.4	1.65	0.24	1.35	1.33	1.25	± 52.5	2.656	2.68	14	133
Total								6.9	7.0		

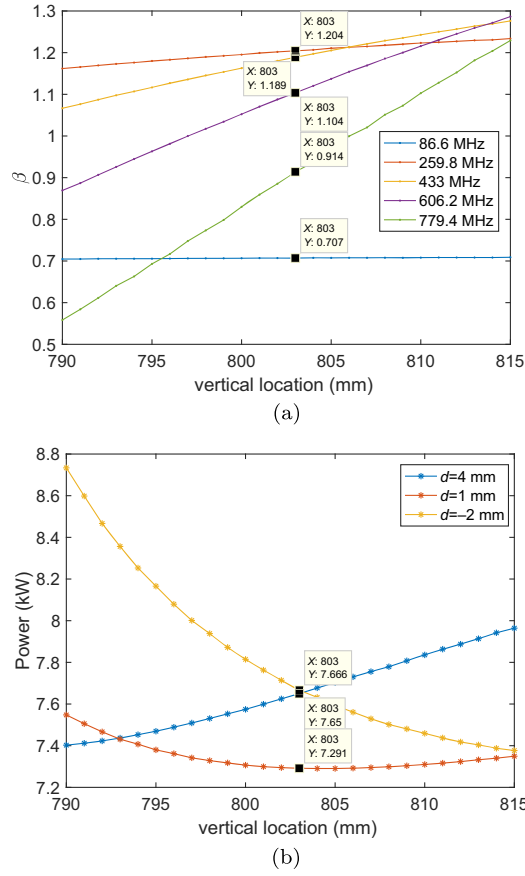


FIG. 10. The optimization of coupler geometry. (a) The β 's of the harmonic modes over vertical position of the coupler port with default insertion of $d = 1$ mm into the cavity. (b) The power over the vertical position of the coupler port with various insertions.

loop, R_{cp} , B_{cp} , H_{cp} , d , w_{loop} , h_{loop} , r_{loop} , l_{gr} , and θ in Fig. 8(b) were scanned in the order of sensitivity to β 's. The most sensitive parameters, the coupler port center location (along the outer conductor of the coaxial line) H_{cp} and the insertion depth d , were scanned simultaneously to obtain convergent couplings (of all the harmonic modes) and the remaining parameters were adjusted to refine the coupling (followed by a few iterations). In Fig. 10(a), the optimal vertical location at $H_{cp} = 803$ mm was chosen near the “crossing” region of the β profiles and the convergent β 's were shifted together by adjusting the depth to $d = 1$ mm. Subsequently, loop width w_l , loop height h_l , and wire thickness r_l were fine-tuned to improve on convergence. The power stability against the field map degradation from fabrication error or misalignment is shown in Fig. 10(b), where one can see the $d = 1$ mm case gives the minimum power and also the most stable over a wide range of vertical location at $H_{cp} = 803$ mm. The power deviations against the insertion errors remain relatively small (7.3–7.7 kW) between $d = -2$ and

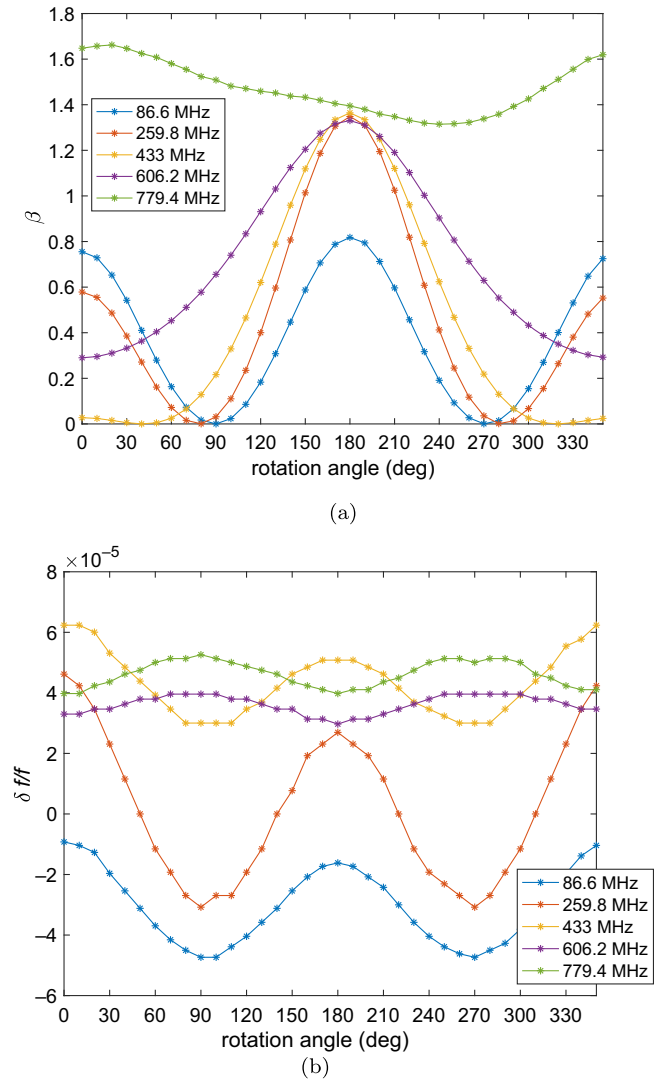


FIG. 11. The coupler loop rotation. (a) The coupling β 's as functions of rotating angle for five harmonic modes. (b) The frequency changes as functions of rotating angle for five harmonic modes.

$d = 4$ mm. Finally, to compensate for the fabrication or installation errors and heating, the coupling can be adjusted to some extent by rotating the loop. The behavior of the coupling over rotation angle is shown in Fig. 11(a) together with very little frequency change 11(b). In Fig. 11(a), the first three modes are magnetically coupled (with the minimum at 90°), while the two higher modes couple electromagnetically. Also, the coupling of the fifth mode is asymmetrical because the topmost tuner port is rotated (by 90°) with respect to the rest of the tuner ports for fabrication issues and the fifth mode is the most sensitive to this change. Due to the position of the loop being far away from the beam axis, there are only negligible changes in the kick field profile with the insertion of the loop (and rotation).

IV. THE RF PERFORMANCE OF THE CAVITY

A. Field profiles

Generic 3D fields of a harmonic kicker cavity are shown in Fig. 12 in a coordinate system as set by the CST-MWS where \hat{z} defines beam axis and \hat{y} is a kick direction. In Fig. 12(a), the electric field of the fifth mode at the phase of 0° is shown to develop the vertically upward kick between the tip of the inner conductor and the bottom. The field is not uniform across the gap and increases from the bottom to the tip. In Fig. 12(b), the magnetic field of the fifth mode is shown from the top view. The field is directed clockwise at the phase of 90° making its contribution to the Lorentz force opposite to the electric fields. For a nontrivial kick with an electron (at the center of the cavity) on-crest of the rf phase, the temporal profile of the electromagnetic fields are $\mathcal{E}(t) = \cos \omega t$ and $\mathcal{B}(t) = \sin \omega t$, respectively, because the phase of B field advances that of E field by $\pi/2$. Notice that, unlike strip line kicker, the kick in a resonant cavity the particle experiences is the same whether the particle is

injected from the left or right beam port (Both \vec{v} and \vec{B} change their signs).

The field profiles on the beam axis, whose only nontrivial components are E_y , B_x , and E_z , are shown in Fig. 13. In Fig. 13(a), the longitudinal profile of each electric mode as seen by a passing electron, i.e., multiplied by temporal profile, is approximately the Gaussian shape. In Fig. 13(b), the magnetic mode resembles the derivative of the Gaussian multiplied by the temporal profile. The longitudinal profile of the transverse Lorentz force, as a sum of the corresponding five harmonic modes is shown in Fig. 14(a), with small deformations in Gaussian shape mainly caused by the magnetic fourth and fifth modes. Notice with a sine function being odd with respect to the origin, the contribution from the antisymmetric B_x field [see Fig. 12(b)] is nontrivial and in the opposite direction to the E_y fields. In Fig. 14(b), total fields for E_y , B_x , and E_z fields are shown. In particular, the profile of a total axial field E_z is antisymmetric with respect to the center [see Fig. 12(a)], and its integration is zero, preserving the energy spread of the electron bunch.

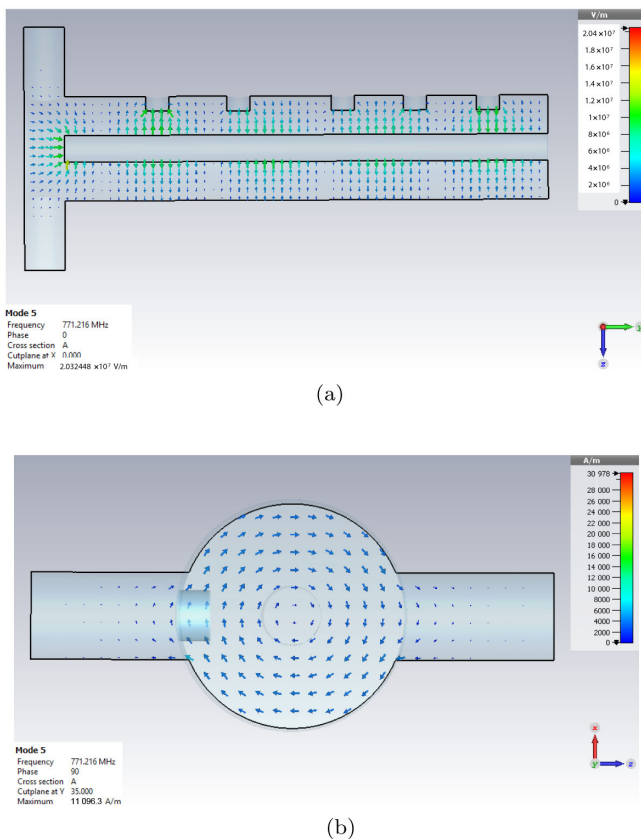


FIG. 12. The 3D field profiles of the QWR. (a) The electric field of fifth mode at 0° phase. The electron is deflected downward. (b) The magnetic fields of fifth mode as viewed from top at phase of 90° . At phase -90° , the electron enters the cavity from the left and the B fields with the counterclockwise orientation deflect the electron upward.

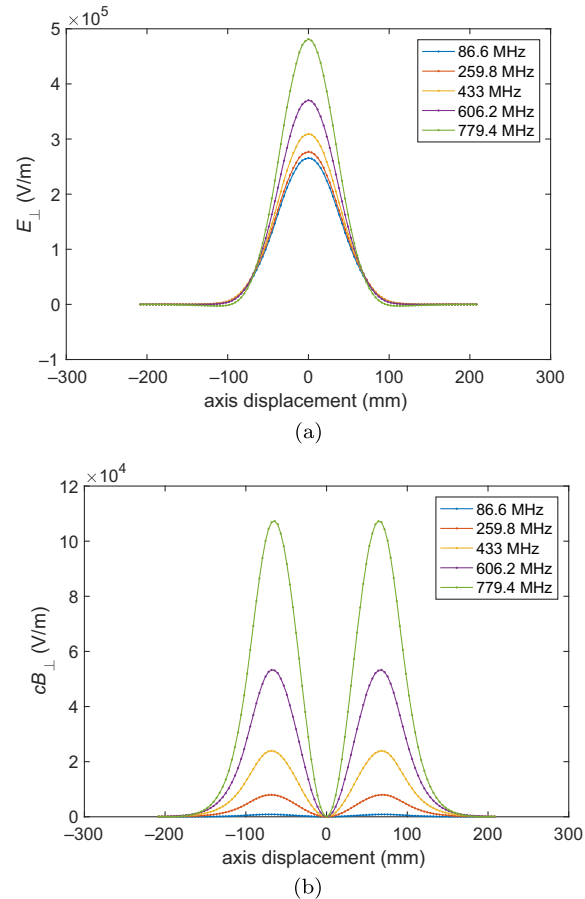


FIG. 13. The longitudinal field profiles of five modes on the axis as seen by a passing electron. (a) The longitudinal profile of electric five modes on beam axis. (b) The longitudinal profile of magnetic five modes on axis.

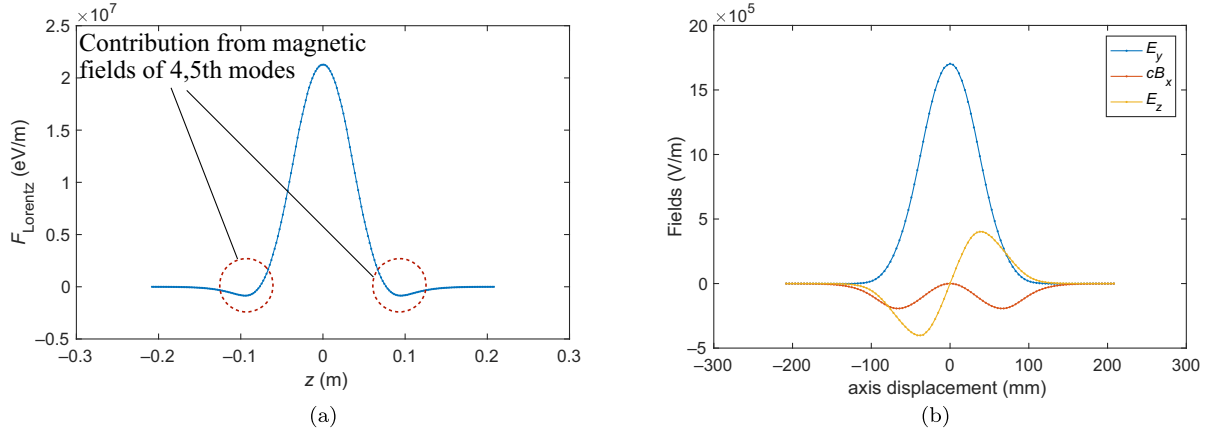


FIG. 14. The field profiles of the QWR. z, x, y are the beam axis, horizontal, and vertical (kick) direction, respectively. (a) The longitudinal profile of the harmonic kick on the beam axis. F_{Lorentz}/q is the Lorentz force per charge as seen by the electron. (b) The longitudinal profile of total fields on axis: E_y, cB_x, E_z fields.

The kick voltage is defined as a line integration of the vertical component of the Lorentz force $\vec{\mathcal{F}}_L$ along the beam-axis:

$$\begin{aligned} V_{\text{kick}} &= \int_{-l/2}^{l/2} dz \mathcal{F}_{L,y} = \int_{-l/2}^{l/2} dz e[\vec{E} + \vec{v} \times \vec{B}]_y \\ &= e \sum_{n=1}^5 \int_{-l/2}^{l/2} dz [E_{y,n}(z) \cos(\omega_n z/c) \\ &\quad + cB_{x,n}(z) \sin(\omega_n z/c)], \end{aligned} \quad (12)$$

where l is an effective length of the cavity and $E_{y,n}, B_{x,n}$ are longitudinal profile of the fields on beam axis.

The power P_g from the generator to keep a constant kick voltage without beam current is given by [14]

$$P_g = \sum_{n=1}^5 \frac{V_{\perp,n}^2 (1 + \beta_n)^2}{R_{\perp,n}} \left\{ 1 + \frac{4Q_{0,n}^2}{(1 + \beta_n)^2} \left(\frac{\delta f_n}{f_n} \right)^2 \right\}, \quad (13)$$

where δf_n is arbitrary frequency deviation and $Q_{0,n}$ is unloaded quality factor for n th mode, respectively. In order to keep P_g reasonably close to the nominal value $P_{g,\text{tot}}^0$ in (11), i.e., $P_g \sim 1.1P_{g,\text{tot}}^0$, the frequency deviations must be controlled as $\delta f_n/f_n \sim 3 \times 10^{-1}/Q_{0,n} \sim 3 \times 10^{-5}$ for all n 's, where δf here refers to the largest allowed frequency deviation defining the resolution of frequency tuning. The figures of merit for the kicker cavity is listed in Table III.

B. Multipole expansion of the field

The effect of the bunch center offset from the beam axis can be described in terms of the multipoles. In Fig. 15(a), the horizontal profile of the kick $E_y(x)$ at $z = 0$ can be considered as constant near $x = 0$ over a few beam sizes. The vertical profile of the kick $E_y(y)$ has some gradient near $y = 0$, indicating the presence of multipole fields. In Fig. 15(b), the rf power with different vertical offsets from the beam axis is shown. The electron on the negative

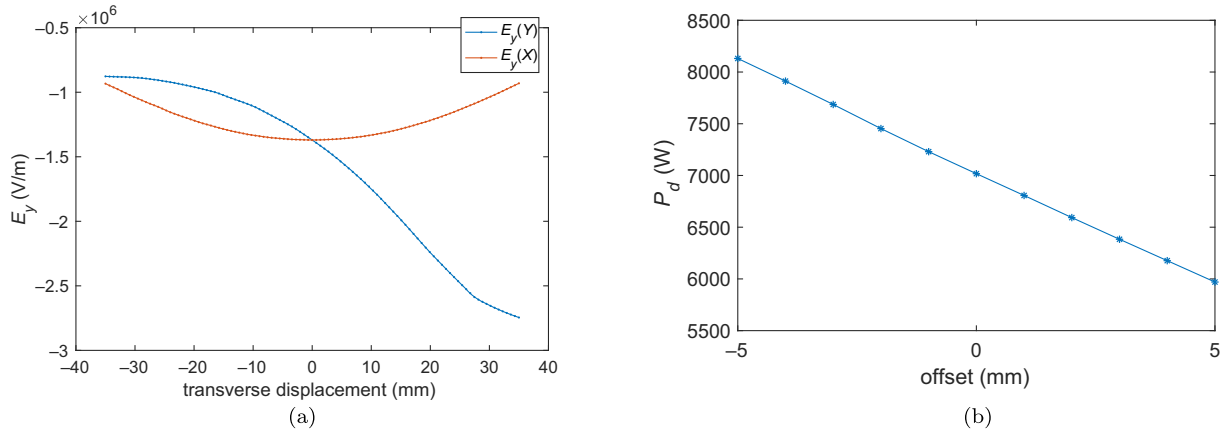


FIG. 15. The transverse profiles of the fields and power as a function of offsets. (a) The transverse profile of the E_y at $z = 0$ for the transverse offsets. (b) The power increase as a function of vertical offset with current coupling due to the multipole fields.

(positive) offset has less (more) transverse kick according to Fig. 15(a), one has lower(higher) shunt impedance and higher (lower) power loss for the nominal kick voltage. The profile is approximately linear over small offsets with the power increase rate of -220 W/mm.

Now we discuss the effects of multipole fields on the kick following [3]. The kick on the bunch can be succinctly described via the Panofsky-Wenzel theorem [17]: the transverse momentum change in kick direction at the exit is expressed in terms of the longitudinal field component E_z . For a generic harmonic mode, we have

$$\Delta p_{\perp} = -\frac{e}{\omega} \int_{-l/2}^{l/2} dz \nabla_{\perp} E_z(\vec{r}_{\perp}, z) \sin \left\{ \omega \left(\frac{z}{c} + \tau \right) \right\}. \quad (14)$$

Here \perp refers to a kick direction, $\Delta p_{\perp} = p_{\perp} - p_{\perp 0}$, where p_{\perp} is the momentum at the exit and $p_{\perp 0} = 0$ is at the entrance, $l = c\beta/f$ is the effective length of the cavity, \vec{r}_{\perp} is a transverse offset vector, and τ is the arrival time of an electron (with respect to the reference electron). Now the integrand in (14) is expanded in terms of multipole fields of E_z around the beam axis (analogous to static magnetic fields, see appendix of [5] for more details). First the complexification \tilde{E}_z of E_z such that $E_z = \Re\{\tilde{E}_z\}$ is expanded at each z over transverse plane in polar coordinates $\{r, \phi\}$ into

$$\tilde{E}_z(\vec{r}_{\perp}, z) = \sum_{n=0}^{\infty} C_n(z) r^n e^{in\phi}, \quad (15)$$

$$\text{where } C_n(z) = \frac{1}{\pi r^n} \int_0^{2\pi} d\phi E_z(\vec{r}_{\perp}, z) e^{-in\phi}. \quad (16)$$

Here ϕ is the azimuthal angle of an offset electron with respect to the kick direction. Then by inserting the real part of (15) into (14) and considering only the offset that is parallel to a kick direction, i.e., $\phi = 0$, the kick in a radial direction is given as

$$p_r = -\frac{e}{\omega} \sum_{n=1}^{\infty} n \Re\{c_n r^{n-1}\}, \quad (17)$$

where complex multipole expansion coefficients c_n 's are defined as

$$c_n = \int_{-l/2}^{l/2} dz \frac{1}{\pi r^n} \left[\int_0^{2\pi} E_z(r, \phi, z) e^{-in\phi} d\phi \right] \times \sin \left\{ \omega \left(\frac{z}{c} + \tau \right) \right\}. \quad (18)$$

The complex coefficients c_n 's are written as $c_n = b_n - ia_n$, where b_n, a_n 's are identified as normal and skew multipole coefficients, respectively. The coefficients in (18) for the QWR are numerically evaluated by inserting the 3D field maps of the E_z , which is obtained from the rf field simulation by the CST-MWS (the details of the accurate evaluation of the 3D field maps in the QWR are found in the appendix of [18]). Finally, if the kick is in y direction, the momentum change (14) can be rewritten as

$$p_y = \frac{e}{c} V_y, \quad (19)$$

$$\text{where } V_y = \sum_{n,m=1}^5 \frac{c}{\omega_m} \Re\{c_{nm} n y^{n-1}\}. \quad (20)$$

Here we included all the harmonic modes (indexed with m) for completeness and c_{nm} refers to the m th order coefficient of the n th mode. The resulting multipole coefficients up to decapole are listed in Table IV. In Table IV, skew multipoles are vanishingly small (compared to normal multipoles) because of horizontal symmetry (with respect to yz -plane) of the fields with $E_z(-\phi) = E_z(\phi)$, while there is no apparent vanishing of even normal multipoles because of lack of vertical anti-symmetry (with respect to xz -plane) in the QWR structure, with

TABLE IV. The multipole field coefficients of a vertical harmonic kick as evaluated based on the circle with 10 mm radius in hexahedral meshing. The coefficients are normalized to kick voltage of 25 kV for each mode.

Multipoles	Mode 1	Mode 2	Mode 3	Mode 4	Mode 5
f (MHz)	86.6	259.8	433	606.2	779.4
b_1 (V)	4.49×10^4	1.37×10^5	2.27×10^5	3.17×10^5	4.05×10^5
b_2 (V/m)	-4.16×10^5	-1.25×10^6	-2.05×10^6	-2.79×10^6	-3.46×10^6
b_3 (V/m ²)	5.33×10^6	1.62×10^7	2.68×10^7	3.75×10^7	4.88×10^7
b_4 (V/m ³)	-3.66×10^7	-1.11×10^8	-1.82×10^8	-2.53×10^8	-3.28×10^8
b_5 (V/m ⁴)	2.08×10^8	6.31×10^8	1.05×10^9	1.48×10^9	2.03×10^9
a_1 (V)	-2.19	3.26	6.76×10	4.07×10^2	2.57×10^3
a_2 (V/m)	8.09×10	4.45×10	-1.18×10^3	-7.86×10^3	-4.99×10^4
a_3 (V/m ²)	-4.48×10^3	-1.10×10^4	-2.71×10^3	6.86×10^4	5.18×10^5
a_4 (V/m ³)	-3.85×10^4	7.80×10^4	-1.03×10^5	-1.28×10^6	-8.80×10^6
a_5 (V/m ⁴)	6.51×10^6	-2.01×10^7	3.54×10^7	6.06×10^7	1.53×10^8

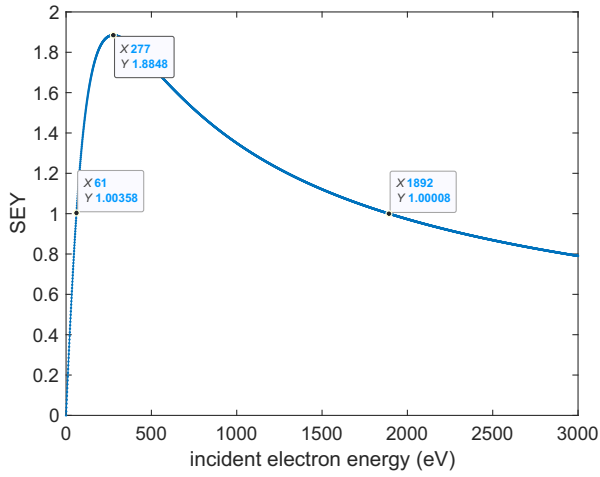


FIG. 16. The SEY curve of the pure copper.

$E_z(\pi - \phi) \neq E_z(\phi)$. Also, notice that the dipole coefficient for each mode agrees with the kick voltage on the beam-axis (upon multiplying c/ω_m 's according to the Panofsky-Wenzel theorem).

Further details on the beam dynamics in the presence of the multipoles are discussed in [3].

C. Multipacting study

The multipacting of the kicker cavity could absorb rf power by forming a current, generate excessive heat leading to a lower (unloaded) quality factor, and damage the cavity surface. In particular, these potential problems could become steady and critical to the operation of the cavity, if the multipacting takes place near the operation voltage. The geometry of the QWR has local resonance structures for possible multipacting: between the inner conductor and the outer conductor (two-point multipacting) and the top plate (two-point multipacting). The resonance in the harmonic kicker cavity is based on the period of the fundamental mode (as the longest period at $T_1 = 11.5$ ns)

even in the presence of all five harmonic modes (whose periods are all subharmonics of T_1). In addition to resonance, multipacting is limited to the electron within the impact energy bandwidth whose corresponding true second emission yield (SEY) > 1 , implying growth of the numbers of secondary electrons. The true second emission yield (SEY) curve as a function of the impact energy of incident electron for pure copper is shown in Fig. 16, where the impact energy bandwidth with (true) SEY > 1 is between 50 eV and 1.8 keV.

The multipacting simulation study was done using the CST-PS (PIC solver). The electromagnetic field from the EM simulation (as a superposition of the five modes as per the prescription in Table I) was imported to the multipacting simulation. To save simulation time and computer memory, the electron sources were localized in two separate simulation runs. The investigation of two-point multipacting at the top plate, where the Lorentz force is dominated by magnetic fields, shows no sign of multipacting over the entire range of the voltage. The investigation of two-point multipacting between the inner and the outer conductor [see Fig. 17(a)] is summarized in Fig. 17. In Fig. 17(b), the overall exponential increase in (normalized) particle number indicates the two-point multipacting with a period of 6 ns (half period of fundamental mode). The multipacting barrier is relatively narrowly defined over 2.5–25 kV, well below the nominal kick voltage of 125 kV. Various well-known techniques to overcome multipacting are available in low voltage regions: rf processing, and jump over of rf voltage to the operation voltage can be applied.

Two-point multipacting across a small gap, where the electric fields are approximately constant across the gap, can be described and evaluated very accurately via analytical formula. For example, this will be applied to the gap between the tuner port and the plungers and between the bottom cap and the outer conductor. The solution to the equation of motion for an electron subject to the electric field as a sum of the harmonic modes is given as

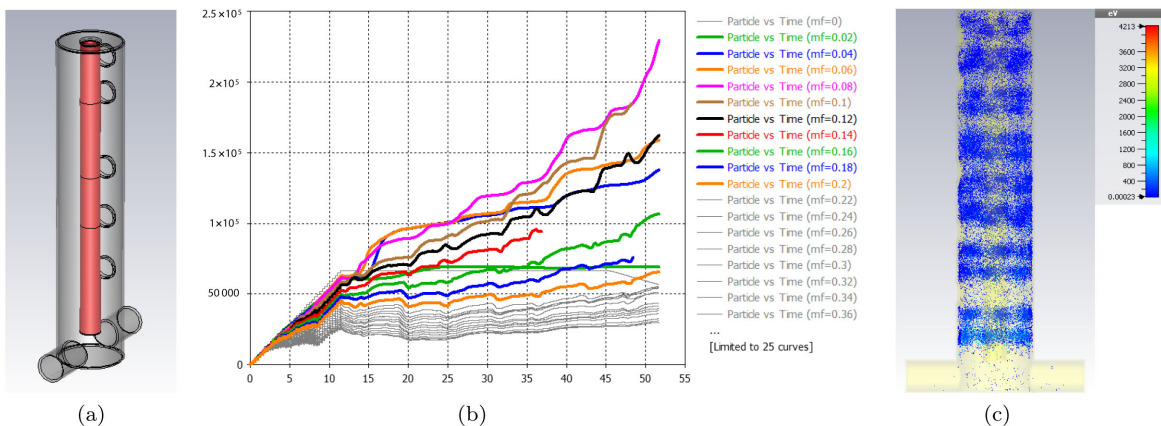


FIG. 17. The multipacting between the inner and the outer conductor. (a) The electron source at the inner conductor. (b) The number of the electrons as a function of time. The colored curves correspond to the multipacting. (c) The trajectories of the multipacting electrons.

$$x(t) = \sum_{n=1}^5 \left[\frac{eE_n}{\omega_n^2 m} \{ \sin(\omega_n t + \varphi_n) - \sin \varphi_n \} - \frac{eE_n}{\omega_n m} t \cos \varphi_n \right], \quad (21)$$

where n is a harmonic number, m is electron mass, E_n , ω_n , φ_n are the peak electric field, harmonic angular frequency, and phase of the n th mode, respectively. The resonance condition is given as that the particle travels the gap distance d in time $\tau = \pi/\omega_1$, i.e., $x(1/2f_1) = -d$. Setting the rf phases $\varphi_n = 0$ for all n in (21), the resonance condition is re-written with the effective voltage across the gap defined as

$$V_{\text{eff}} = \sum_{n=1}^5 \frac{E_n d}{(2n-1)} = \frac{4\pi m d^2 f_1^2}{e}. \quad (22)$$

The second equality is by using the resonance condition. Furthermore, the impact velocity of an incident electron can be computed by differentiating (21) to be $\dot{x}(1/2f_1) = -eV_{\text{eff}}/(m\pi f_1 d)$. Then nonrelativistic kinetic energy K is given as

$$K = \frac{e^2 V_{\text{eff}}^2}{2\pi^2 m f_1^2 d^2} = 8m f_1^2 d^2, \quad (23)$$

which needs to be between 50 eV and 1.8 keV in copper SEY (according to Fig. 16) for $\text{SEY} > 1$. With $d = 1$ mm, $K = 0.34$ eV only.

V. MECHANICAL DESIGN FOR FABRICATION

For a high power operation of the cavity up to 7.1 kW, the mechanical design of the cavity is focused on

implementing a water cooling scheme that limits thermal loads to the cavity system and controlling the frequency shifts due to various deformations of the cavity geometry during the installation and operation. The frequency deviations before the installation to the beamline can be handled via a target frequency table, while the deviations left over after the final welding or during the operation are to be compensated by the tuners with the aforementioned tuning range. As a part of the engineering design, the minor modification in cavity geometry includes: the bottom cap was introduced to give an additional frequency control other than the stub tuners, open access for chemical polishing, and also for easier handling during the fabrication. The top tuner port was rotated by 90° in order to avoid the interference of the step motor station mounted on the tuner ports. Due to the axial symmetry of the fields around the inner conductor, the tuning range with this rotation remained the same.

A. Thermo-structural analysis

A thermo-mechanical analysis for a cooling system design for a high-power operation was done with a series of coupled multiphysics simulations using the CST-MPS (for a more detailed analysis using the ANSYS [19], see [20]). In the analysis, the total rf power loss on the (inner) surface of 4 mm thick cavity wall [see Fig. 18(a)] at full power was imported into the thermal simulation as the thermal loads and the temperature distribution was computed. The power computed in the rf simulation is based on a constant surface resistance (at the fixed temperature) of the pure copper, not taking into account positive feedback where the temperature, resistance, and power are all dynamic variables depending on one another. The analysis with the temperature-dependent resistance would require a number of

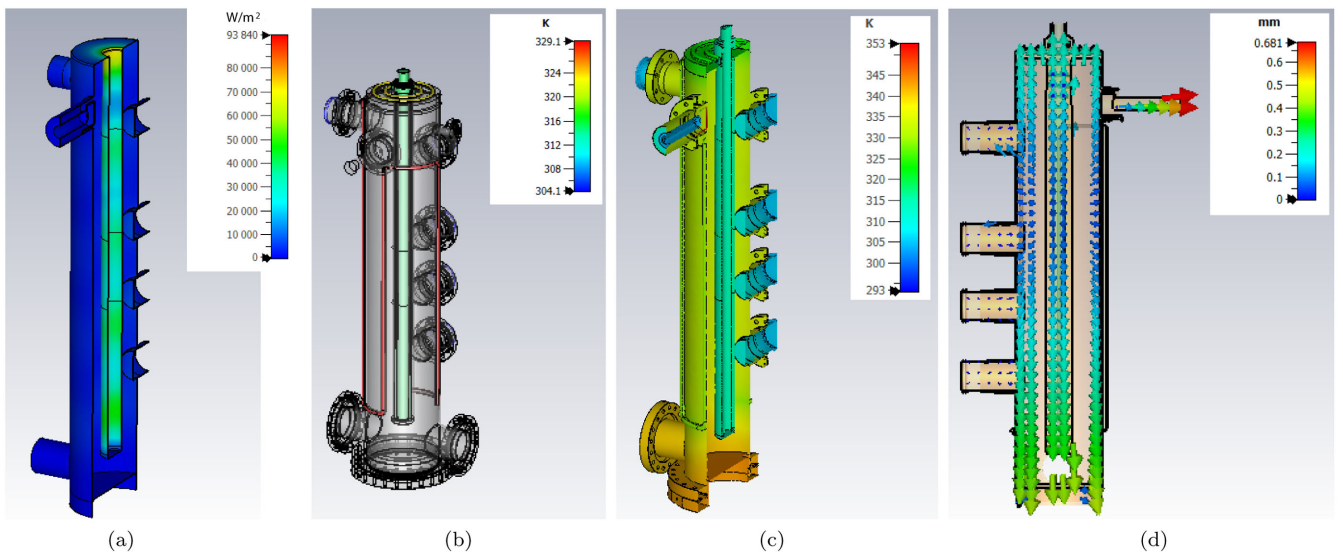


FIG. 18. The thermal analysis at 7.5 kW. (a) The rf power distribution. (b) The temperature of the cooling water in equilibrium. (c) The temperature distribution. (d) The deformation of the cavity.

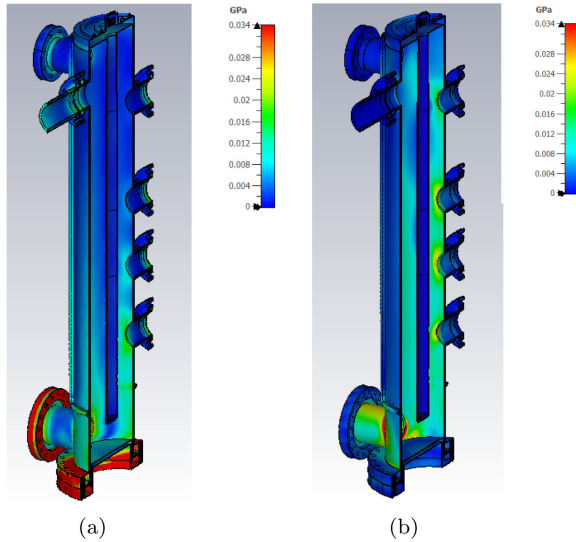


FIG. 19. The mechanical stress analysis. (a) The Von mises stress by thermal load at 7.5 kW. (b) The Von mises stress by evacuation.

iterations in the simulation runs until the saturation in the temperature is observed. Here we limit the validity of the current analysis to a constant temperature close enough to the saturated temperature. After finding out the cavity temperature is too high over $\sim 100^\circ\text{C}$ without a cooling water system but only with the air convection around the outer conductor, which would lead to unstable temperature fluctuations during operation, cooling water channels were implemented inside the inner conductor—the inner conductor was the hottest mass with the strong magnetic field. A total cooling water flow of 1.25 l/min at an inlet temperature of 30°C runs down a single channel before branches at the bottom into three channels sized to promote a turbulent flow while maintaining a transitional flow at supply pipes. To reduce the temperature further down, additional water channels were also implemented over the top plate, around

the outer conductor, and the back end of the stub tuners as shown in Fig. 18(b). In particular, a cooling water channel was introduced inside the inner conductor of the coupler. The resulting temperature profile at full power is shown in Fig. 18(c). Except for the localized hot mass of the coupler loop at 80°C , the bulk of the cavity body remains at around $60\text{--}70^\circ\text{C}$. The hottest region of the body at 70°C is near the bottom where the cooling water does not reach. The temperature of the inner conductor of the coupler is controlled at 30°C and would be in direct thermal contact with a ceramic window, which was demonstrated to withstand the temperature over 100°C at 14 kW power [21].

For structural stability, stress and modal analysis were done. The stress analysis for thermal expansion and evacuation are shown in Fig. 19. Given that the yield strength of the copper and the stainless steel (304) is 33.3 and 205 MPa, respectively (the ultimate strength of the copper is 210 MPa), the von Mises stresses on the cavity in Fig. 19 are mostly below the yield strength and the ones that exceed the yield strength are in either stainless steel flanges (thermal load stress) or localized around the beam pipe joints (evacuation stress), where the fixed boundary constraints affect the most.

The result of the modal analysis to obtain vibrational resonant frequencies is listed in Table V. All the resonant modes are found between 15–64 Hz, which overlap with the external microphonics from the vacuum pumps. However, the microphonics transfer function for a typical QWR suggests that the resulting rf frequency shifts are a few tens of Hz [22,23]. In particular, the top plate was reinforced by using a thicker wall, which reduced the vibration amplitude of the inner conductor (pendulum modes) found at $\sim 36\text{--}39\text{ Hz}$ in Table V.

B. The heating on the stubs

An engineering design of the stub tuners has a 1 mm gap between the stubs and tuner port [see Fig. 20(a)] as a

TABLE V. The modal analysis of the kicker cavity: mechanical vibrational eigenfrequencies.

Mode	f (Hz)	Behavior
1	17.6	sway of the entire assembly toward tuners
2	20.8	twist of assembly about the axis, induced by tuners
3	26.4	counter twist of tuners about axis
4	32.5	counter twist of tuners about axis
5	35.1	twist of tuners, the pendulum of inner conductor along beamline
6	36.2	pendulum of inner conductor transverse to beamline
7	36.8	counter twist of tuners about axis
8	38.9	twist of top tuner, the pendulum of inner conductor along beam line
9	43.7	twist of top tuner about axis
10	52.4	tuners pitching
11	53.3	tuners pitching
12	53.9	tuners pitching
13	60.9	tuners pitching
14	63.5	tuners pitching

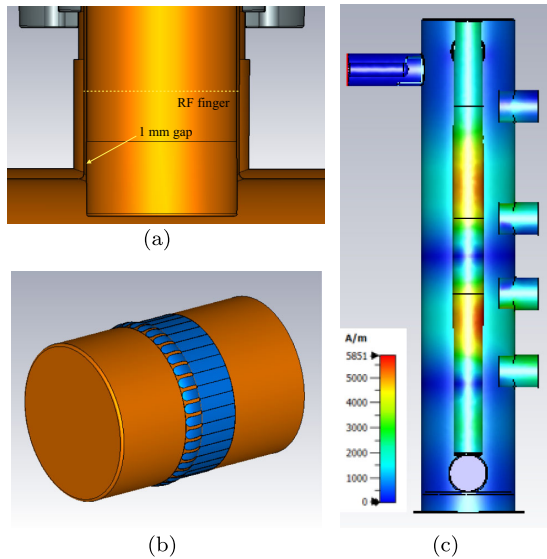


FIG. 20. The designs and the fields of the tuners. (a) The plunger with a gap. (b) The rf finger wrapped around the stub. (c) The magnetic field distribution.

clearance for moderate misalignment error, through which the resonant rf modes could leak.

If the rf coupling of any mode at the stub allows the leaked fields to form TEM modes, then the mode could propagate through the back of the port (without cutoff) to form standing waves, leading to significant rf heat loss. The condition for standing wave is roughly given as

$$l_{\text{eff}} = \frac{\lambda_n}{4} (2k - 1) = \frac{\lambda_1}{4(2n - 1)} (2k - 1),$$

for some $k \in \mathbf{Z}$ and $n = 1, \dots, 5$, (24)

where l_{eff} is an effective length associated with the stub configuration and λ_n is wavelength of n th resonant mode. The integers $2k - 1$'s correspond to odd multiples of the

wavelength (25) that can form standing waves. The shortest l_{eff} that allows the standing wave for the ninth harmonic (with the shortest wavelength) with $k = 1$ is $l_{\text{eff}} = 96.2$ mm, which should be considered to be the upper limit on the length of the tuner ports. If we consider higher order modes excited by a high beam current, 952.6 MHz mode in particular, we would have 78.7 mm for l_{eff} .

We investigated the heating in the gaps of tuner ports, determining the appropriate port lengths and the relevance of the rf finger [shown in Fig. 20(b)], which blocks the rf modes from leaking through the gaps in the ports. The focus was on the second and the third ports (from the bottom), where the magnetic field is strong, as illustrated in Fig. 20(c). In Fig. 21(a), the port length is varied with the stub in nominal position, i.e., 15 mm into the cavity, while the total power on each stub (by a sum of five harmonic modes) was tracked. The plots show that the power loss starts to pick up drastically (to ~ 10 kW) around 95 mm. The power profiles are dominated by the contribution from the fifth mode, as demonstrated by the fifth mode magnetic energy density around the ring at the back of each port also picking up near 95 mm in Fig. 21(b). This implies the standing wave formation for the ninth harmonic. Both plots show the curves head down past 95 mm and pick up again around 120 mm, which corresponds to the standing wave condition (25) with $k = 2$. With many mechanical constraints imposed on the tuner port, it is difficult to obtain port length shorter than 90 mm, and the rf finger at 45 mm [see Fig. 20(a)] is introduced for the minimum power loss by blocking rf fields, as suggested in [24]. Furthermore, when the stubs are in motion for tuning, the effective length l_{eff} in (25) changes (because the field configuration near the opening of the gap changes accordingly), and it may be impossible to avoid standing wave formation for all five modes in all five ports under general circumstances. This was checked by a series of simulations with stubs insertion scanned as shown in

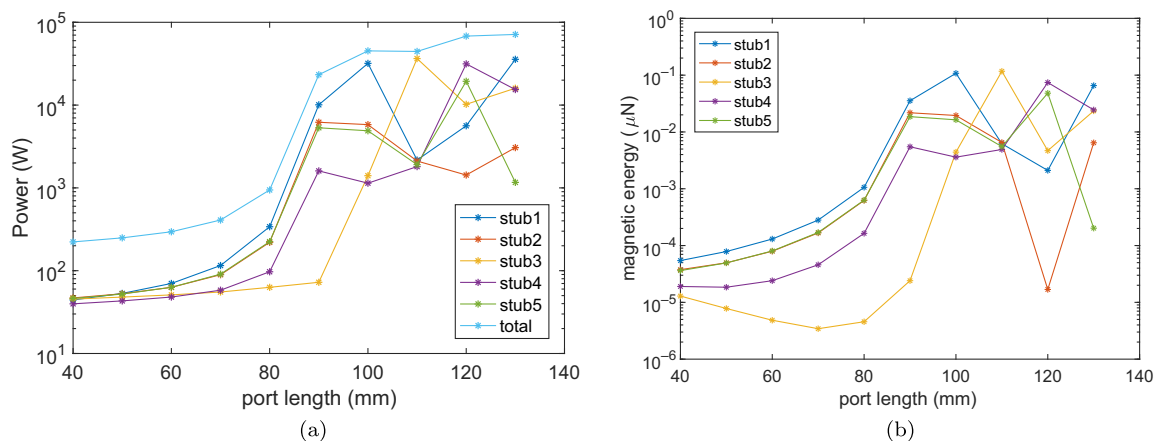


FIG. 21. The power on the stubs vs port length. (a) The rf power on the plungers at nominal positions. (b) The integrated magnetic energy density of the fifth mode over ring area on the back flange.

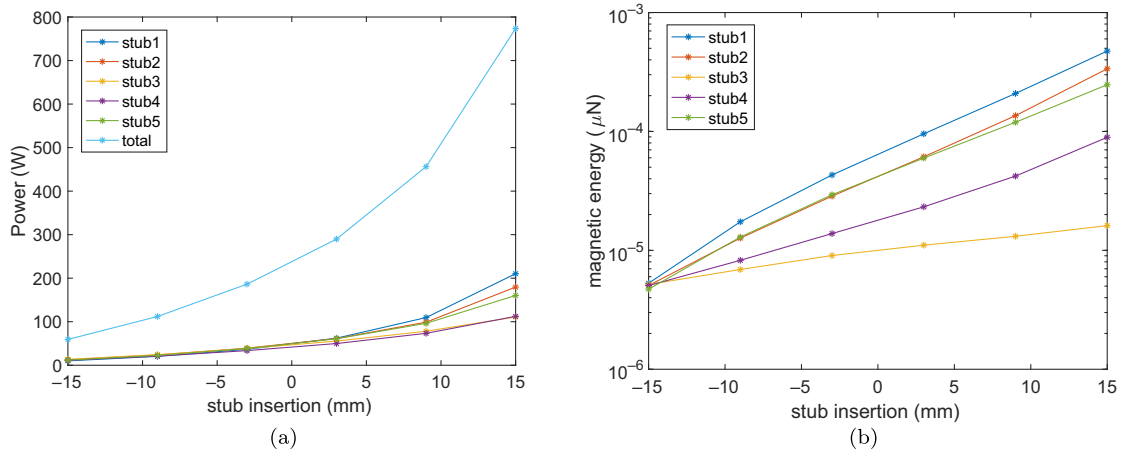


FIG. 22. The total power on each stub vs insertion. (a) The power on the stubs vs insertion. The contributions from all the modes are summed up on each stub. (b) The integrated magnetic density of the total modes over ring area on the back flange.

Fig. 22. The simulation of the plunger travel within the tuning range shows no development of the TEM modes, but instead gradual power increase as the stubs near the inner conductor, where the magnetic fields are stronger. Note that even after the installation of the fingers, the modest amount of rf leakage still could exist (up to ~ 45 mm, the location of the finger) as TM mode in the gap, but the mode exponentially decays. Finally, the two-point multipacting in the gap is unlikely, according to the incident electron energy that satisfies the resonance

condition as calculated by (23): 0.34–27.5 eV, far below multipacting range in Fig. 16.

C. Target frequency table

From trimming in the bench test to beamline installation, the frequencies of the cavity can be controlled by achieving the target frequency at each step listed in Table VI. The target frequencies were set for the actual beam test at the UITF. During the evacuation, there exist two different mechanisms for the frequency shifts. One is

TABLE VI. The target frequency table for the beam test benchmarked with the measurements. The numbers in the parenthesis are simulated target values.

Procedures	86.6 MHz	259.8 MHz	433 MHz	606.2 MHz	779.4 MHz
Baseline trimming					
δf (kHz)/mm	100 (101)	286 (304)	537 (515)	682 (699)	924 (878)
Final joint					
f (MHz)	86.605	259.596	432.982	606.157	779.005
Assembly for evacuation					
f (MHz)	86.5925 (86.585)	259.6300 (259.760)	433.0046 (432.932)	606.3228 (606.104)	779.4237 (779.277)
Evacuation					
δf (kHz)	18.1	53.1	33.5	5.3	56.3
Dielectric constant	(25.547)	(76.641)	(127.735)	(178.829)	(229.923)
Deformation	(-0.57)	(-1.00)	(-2.45)	(-3.26)	(-5.86)
Sum	(24.977)	(75.641)	(125.285)	(175.569)	(224.063)
f (MHz)	86.6106 (86.610)	259.6831 (259.835)	433.0381 (433.057)	606.3281 (606.279)	779.4800 (779.501)
Thermal heating					
δf (kHz)	-8.725 (-6.6)	-18.26 (-25.2)	-69.35 (-40.6)	-54.93 (-56.3)	-67.97 (-71.5)
f (MHz)	86.6019 (86.603)	259.6648 (259.810)	432.9688 (433.017)	606.2732 (606.223)	779.4120 (779.430)

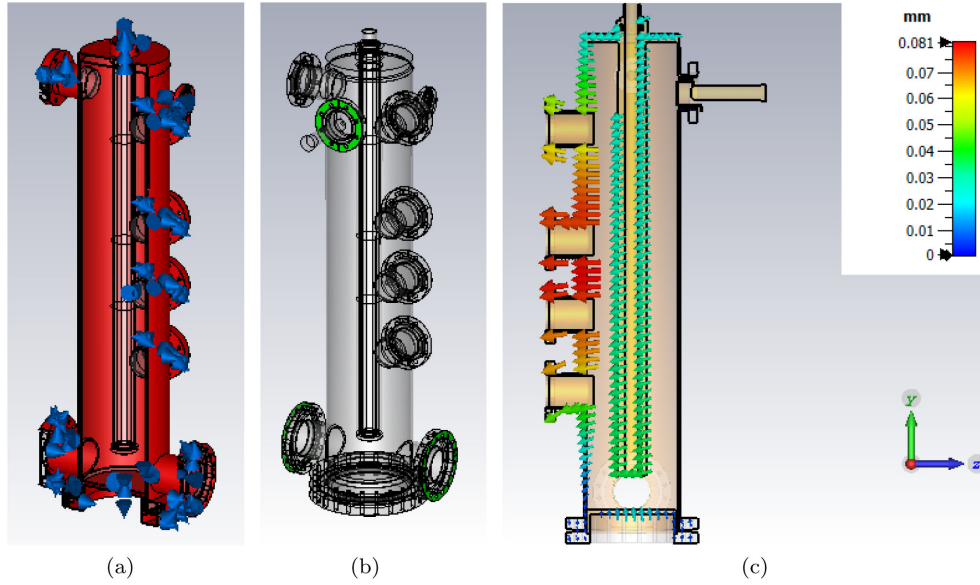


FIG. 23. The evacuation multiphysics simulations. (a) The atmospheric pressure (1 bar) on the cavity wall. (b) The fixed boundary conditions on the beam and coupler ports. (c) The displacement. Due to the fixed coupler port and the pressure inside the inner conductor, the dominant displacement is the one toward the stubs. The more relevant displacement is shrinkage.

via the change in dielectric constant from air to vacuum. The other is mechanical deformation. For the dielectric constant change, the frequency change is given as

$$\frac{\delta f_n}{f_n} = -\frac{1}{2} \frac{\delta \epsilon}{\epsilon}. \quad (25)$$

$\delta \epsilon = \epsilon_{\text{vac}} - \epsilon_{\text{air}} = 1 - 1.00059 = -0.00059$ (at STM, 0.9 MHz), $\delta f_n/f_n = 2.95 \times 10^{-4}$. The frequency shift due to mechanical deformation is obtained by coupled simulations using CST-MPS and CST-MWS. With the fixed boundary condition on the beam and the coupler ports, the pressure difference of 1 bar was applied to the shell deformation as shown in Fig. 23(a). The maximum deformation is at the tuner ports, as shown in Fig. 23(c).

The frequency shift due to “free” (without any mechanical constraint) thermal expansion by rf heating would be analytically estimated as

$$\frac{\delta f_n}{f_n} = -\frac{\delta l}{l} = -\kappa \Delta T, \quad (26)$$

where $\kappa = 16 \times 10^{-6}/\text{K}$ is the thermal expansion coefficient for the oxygen-free copper (OFC) and ΔT is the temperature difference. The expected cavity body temperature difference between evacuation at room temperature and the onset of a water cooling system (whose temperature is fixed by a chiller at 30 °C) during the actual beam test was 6 K—the test was done with low power at around 150 W and the body temperature was the same as the water temperature. Notice that the

temperature difference is much smaller than our default full power operation scenario with 7.1 kW power, where the difference is $\Delta T = 45$ K. The expected frequency shift for the test is computed to be $\delta f_n/f_n = 9.6 \times 10^{-5}$. This estimate is slightly different from the simulated frequency shift (see Table VI), which is based on the expansion with the fixed boundary condition on the beam pipe applied in the simulation. Figure 18(d) shows the thermal expansion with fixed beam and coupler ports. The target frequency at each step, based on the estimation by simulations, is tabulated in Table VI.

VI. PROTOTYPE FABRICATION

A prototype cavity for high vacuum, high power operation was fabricated with mostly 4 mm thick OFC. Two subassembly groups were fabricated in parallel, clamped up for an rf bench test, and finally joined leak-tight by the TIG braze. The cavity surface was supposed to be chemically polished after the final joining by the electron beam welding (EBW), but the TIG braze was done instead and the surface was polished only before the clamp-up.

A. Fabrication of subassemblies

The fabrication of two subassembly groups, the outer tube, and the inner conductor group, went parallel with separate controls on the part dimensions and vacuum leakage. The outer tube group started with a machined 4 mm thick copper tube, and various ports were brazed to the tube in a high vacuum furnace in multiple stages. The brazing of the ports were grouped into four batches using

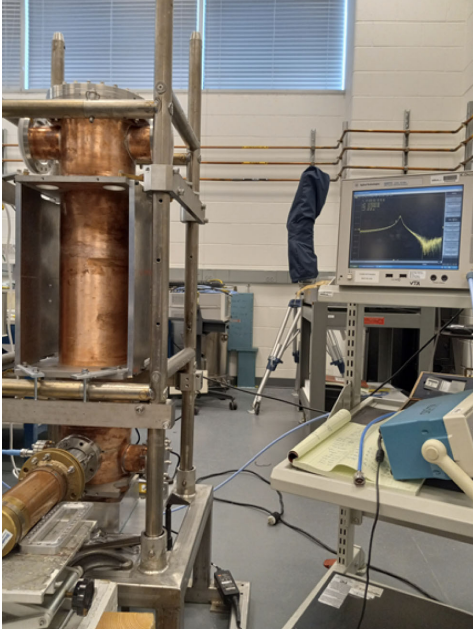


FIG. 24. The kicker cavity placed in the cage for the bench test. Its orientation is upside down for measurement convenience.

the filler alloys with different (in a decreasing order) melting temperatures. The braze work softened the copper and deformed the tube and ports with some dimensional errors. The inner conductor group started with a high-accuracy computer numerical control (CNC) machining of tapering slopes on a solid cylinder, a thickened top plate to prevent the inner conductor from oscillating, water channels, and inner conductor cap, which was separated from the inner conductor for an easy trimming during the clamp-up test. A top plate and a cooling channel were electron beam welded to the tapered cylinder—the inner conductor cap was welded to the inner conductor before a final joining. Throughout the procedure, dimensional checks were done with a coordinate measuring machine (CMM)/optical scanner (FARO). Special attention was focused on the dimensional control of the high frequency-sensitivity regions of the cavity where the electromagnetic fields are strong, i.e., near the top plate and the gap. Moreover, the inner conductor was centered to preserve the multipole structure of the fields. The rf finger made of Cu-Ni-Sn alloy [24], coated with silver (protection against galling), was mounted onto each tuner flange to be inserted into the gap (between the tuner port and the plunger) to stop the rf leakage. Subsequently, the surfaces of the subassemblies were polished by the Copper-brite. After leak checks, the completed subassemblies are shown “clamped” up and caged in Fig. 24 set for the rf bench test.

B. The clamp-up test and final welding

The nominal rf frequencies of the kicker cavity at its operation are controlled step by step during the

installation because both the fabrication and installation procedures would inevitably involve frequency changes. Table VI lists “the target frequency” that needs to be achieved after each step. In particular, the frequency deviations due to fabrication errors can be assessed and compensated (to some extent) via a clamp-up test. In the test, the subassemblies were clamped up (the setup for the test is shown in Fig. 24) before the final joining and the designated region of the cavity—the outer tube, the inner conductor cap, and the “top hat”-flange had been prepared with extra 2–4 mm margin in length—was trimmed away while the frequency changes (increases) were tracked as the targets are gradually approached from below.

The measurements of frequencies are tracked through various trimmings/final joining steps and summarized in Fig. 25. All the measurements were done with an extra 2 mm thickness on the top hat-flange surface (reserved for final fine-tuning after a final joining). Once the gap distance is to the nominal design value (at step 2 in Fig. 25), one obtains a linear fractional frequency response rate against a “baseline” trimming, i.e., a pair of cuts on both the outer and the inner conductor cap by the same amount (1 mm). The baseline trimming keeps the gap distance constant. The rate is used to determine the final trimming length to reach the target frequency. The prediction of the response rate based on the simulation is $\delta f/f \sim 1.2 \times 10^{-3}/\text{mm}$ for all five modes. This implies that, unlike a single-frequency cavity, the trimming of a harmonic kicker cavity can shift all the frequencies by the same fraction, but cannot reduce the spread among the frequency fractions of the

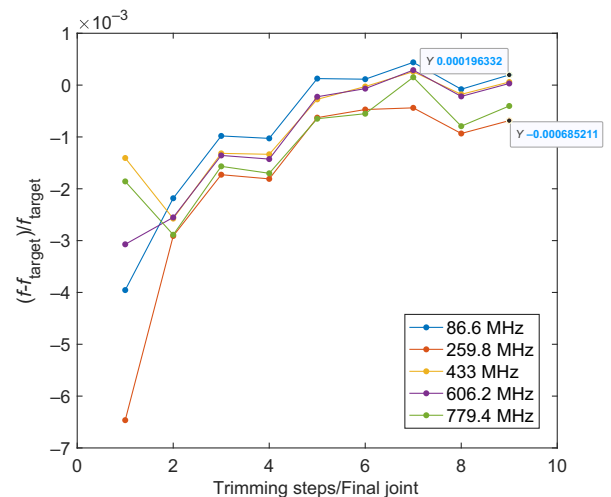


FIG. 25. The tracking of fractional frequencies of harmonic modes throughout various trimmings/final joint steps: (1) initial assessment, (2) 1.5 mm cut on the outer, (3) 1 mm on the inner, (4) 1 mm cut on the outer, (5) final cut on the inner (1 mm) and the outer (1.2 mm), (6) after EBW on the inner cap, (7) S-bond, (8) TIG-braze, (9) 3 mm cut on the top hat flange.

TABLE VII. The rf coupling and (unloaded) quality factor measurements. Here β was computed as $\beta = (1 \mp S_{11,\min}/S_{11,\max}) / (1 \pm S_{11,\min}/S_{11,\max})$ where upper(lower) sign corresponds to the over/under coupling. The values in the parenthesis refer to the nominal design values.

Mode	1	3	5	7	9
f (MHz)	86.6098 (86.603)	259.7992 (259.810)	432.9878 (433.017)	606.2005 (606.223)	779.4521 (779.430)
Q_L	3659 (3293)	5030 (4494)	6729 (11432)	6711 (6957)	5613 (7425)
$ S_{12} $ (dB)	41.4	36.3	36.4	37.4	38.8
S_{11}^{\min} (mU)	314.8	96.44	54.6	40.7	177.4
S_{11}^{\max} (mU)	978.4	998	983.9	957.9	922.7
Coupling	under (under)	under (over)	over (over)	over (over)	over (over)
β	0.51 (0.74)	0.82 (1.21)	0.88 (1.22)	1.09 (1.20)	1.49 (1.25)
Q_0	5525 (5700)	9154 (9800)	11804 (12800)	14026 (15100)	13976 (16500)
Q_{ext}	10834 (7800)	11164 (8300)	13414 (10700)	12868 (12900)	9380 (13500)
Q_{fp} (10^7)	6.9	3.9	5.1	7.6	10.1
β_{fp} (10^{-4})	0.80	2.4	2.3	1.8	1.4
G	(15)	(43)	(77)	(107)	(133)
σ_c (10^7 S/m)	4.64	4.65	4.02	4.11	3.40

modes, leaving the fine-tuning to stub tuners. The baseline trimming (steps 3 and 4) measurement perfectly agrees with the simulation prediction. The final cut was determined taking into account the welding shrinkage (~ 0.1 mm) of the inner conductor cap and the extra thickness of the top hat-flange so that the final fractional frequency deviations (at step 9) are centered to 0 within the expected tuning range.

In addition, the rf couplings and Q_0 were also measured and benchmarked against the simulated prediction. Before the final joint, except for the first mode that has a very good agreement with the simulated prediction, the other modes have rather poorer agreements on both the rf couplings and (unloaded) quality factors Q_0 (lower than expected). We believe this is due to poor rf contact inside an (improved, no vacuum-tight) mockup coupler and on the final joint as well as lower copper conductivity of dirty rf surface.

An option for the final joint between the two sub-assemblies went through a series of changes: the electron beam welding (EBW), whose welding parameters for consistent performance on the full-penetration were not obtained, was replaced by a ‘‘S-bond’’ technique, low-temperature brazing [25]. S-bond failed to make the cavity leak-tight and was replaced by a TIG-braze, which made the cavity leak-tight but without full penetration. In Fig. 25, although events 7 and 8 were not supposed to change the frequencies (without shrinkage), the measurement shows there were some significant frequency changes, which forced the top-hat flange trimming bigger

than the planned 2 mm. This changes the multipole structure of the kick profile. After chemical polishing, the TIG-braze, and the implementation of a vacuum-tight input coupler, Q_0 increased significantly and the rf coupling improved to near nominal values (see Table VII). After the TIG-braze, the top hat flange surface was trimmed off (at step 9) to finalize the frequency tuning, which put all the five modes between -6.85×10^{-4} and $+1.95 \times 10^{-4}$, which is within tuning range even before tuning by a tuning system. After the completion of the cavity fabrication, the cavity was evacuated and tested to be leak-tight. Finally, the cavity was installed onto the beamline and connected to a cooling water whose temperature was fixed to $30^\circ \pm 0.5$ C. The measured frequency change through these two steps are also listed in Table VI.

VII. THE RF TEST OF A CAVITY

A. The measurements of the tuning matrix

The tuning matrix elements for stub tuners were measured with all the stubs at the nominal positions (15 mm into the cavity volume). During the measurements, the frequencies were measured before/after the insertion of the stubs by dialing the rotating knobs. The repeatability of the frequency response to the insertion was checked with a caution given to reversing the tuning knob rotation. The matrix elements $[\mathcal{T}_{\text{stub},0}]_{ij}$ ($i, j = 1, 2, \dots, 5$) in (27), obtained from the measurements, correspond to the frequency change (in MHz) of the i th mode against the j th plunger insertion by 1 mm. In comparison with the simulated prediction (the numbers in parenthesis), the elements involving lower-order modes are almost identical, while those involving higher-order modes have some small discrepancies. The discrepancies are mostly from the misalignment of the stub insertion, which was complicated in the presence of the rf finger.

$$\mathcal{T}_{\text{stub},0} = \begin{bmatrix} -0.018 & -0.011 & -0.003 & 0.008 & 0.010 \\ (-0.019) & (-0.012) & (-0.003) & (0.008) & (0.011) \\ 0.007 & 0.026 & -0.045 & -0.030 & 0.020 \\ (0.005) & (0.025) & (-0.043) & (-0.034) & (0.021) \\ 0.048 & -0.112 & 0.038 & -0.105 & -0.007 \\ (0.047) & (-0.114) & (0.032) & (-0.116) & (0.003) \\ -0.060 & 0.038 & -0.165 & -0.086 & -0.034 \\ (-0.068) & (0.035) & (-0.159) & (-0.094) & (-0.045) \\ -0.199 & -0.090 & 0.085 & 0.030 & -0.099 \\ (-0.226) & (-0.099) & (0.076) & (0.029) & (-0.121) \end{bmatrix}. \quad (27)$$

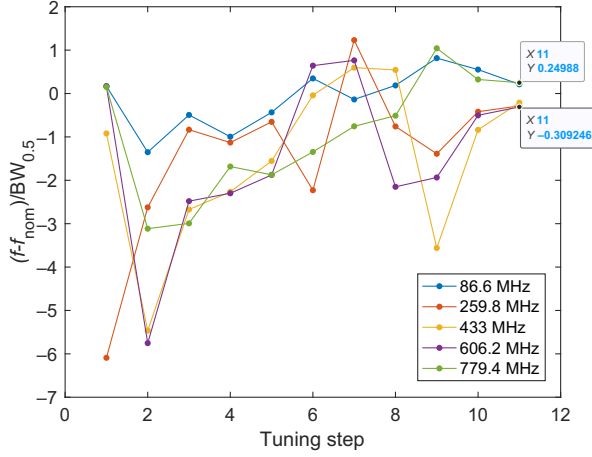


FIG. 26. The tuning of harmonic modes.

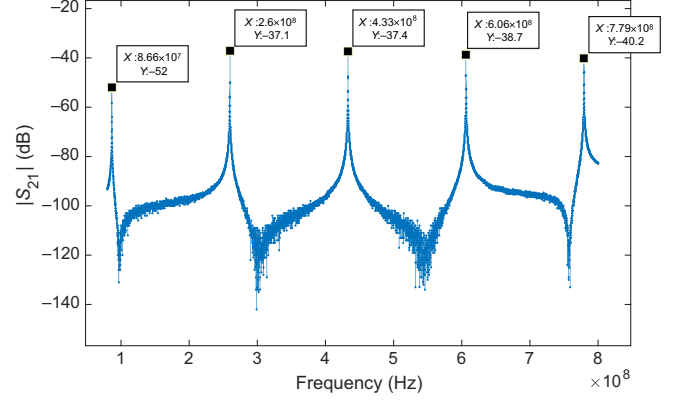
In a linear tuning regime, this close overall agreement would lead to a (fractional) frequency tuning range of 5×10^{-4} (for all five modes), as predicted by the simulation. The tracking of the actual frequency deviation of the cavity as the tuning scheme was applied is shown in Fig. 26. The initial deviation was big enough for a linear tuning scheme to break down—after some iterations with a tuning matrix $\mathcal{T}_{\text{stub},0}$ in (27), the frequencies were not improving at all with further iteration (tuning steps 6–8 in Fig. 26). Taking into account nonlinear frequency response, another tuning matrix $\mathcal{T}_{\text{stub},1}$ in (28) had to be evaluated at the stagnant point (tuning step 9 in Fig. 26) before tuning to the nominal frequencies much more effectively. The final tuned frequency deviations were within ± 0.3 bandwidths, which was mostly limited by the mechanical accuracy of dialing the tuning knobs (up to 0.05 mm).

$\mathcal{T}_{\text{stub},1}$

$$= \begin{bmatrix} -0.0124 & -0.0166 & -0.0052 & 0.0059 & 0.0124 \\ 0.0070 & 0.0290 & -0.0580 & -0.0160 & 0.0230 \\ 0.0390 & -0.1580 & 0.0370 & -0.0630 & -0.0030 \\ -0.360 & 0.0360 & -0.2160 & -0.0440 & -0.0690 \\ -0.1340 & -0.1710 & 0.0870 & 0.0290 & -0.1800 \end{bmatrix} \quad (28)$$

B. The measurement of rf parameters

The rf parameters were measured after the final joint to determine the rf coupling β 's and the quality factors as well as the resonant frequencies. The frequency spectrum (S_{12}) for the five harmonic modes is shown in Fig. 27 (also listed in Table VII), whose frequency

FIG. 27. The frequency spectrum of $|S_{21}|$ from the vector network analyzer (VNA) showing the peaks at the resonant frequencies of a kicker cavity.

deviations from the nominals are all well within the half-bandwidths.

The rf couplings and quality factors, as obtained from S_{11} measurements (port 1 is the input power coupler), are listed in Table VII. They are in good agreement with the nominal values except for the ninth harmonic. To understand the discrepancy in the ninth harmonic, Assuming geometry factors G of the actual cavity—they are not directly measurable—are close to the simulated values, the conductivities σ_c of the copper on the cavity surface can be derived from the measurement-based Q_0 's mode by mode as per (29) and were listed in Table VII.

$$\sigma_c = \frac{\pi f \mu_0}{R_s^2}, \quad \text{where } R_s = \frac{G}{Q_0}. \quad (29)$$

Here $\mu_0 = 4\pi \times 10^{-7}$ N/A² is vacuum permeability and R_s is the surface resistance of the copper. Given that all the simulated nominal figures of merit in Table VII were based on the default value of $\sigma_c = 4.8 \times 10^7$ S/m, the derived conductivities are to be compared to the default value. The comparison implies there exists a significant reduction in conductivity to varying degrees depending on the frequencies of the modes. The reduction is believed to result from surface contamination during the S-bond and lack of chemical cleaning after TIG braze, which led to a rougher surface. It is well known [26,27] that the surface roughness reduces conductivity and the reduction is bigger with higher frequency modes. On the other hand, the discrepancy in Q_{ext} could be traced back to the fabrication/installation errors of the (coupler) antenna configuration, to which the ninth harmonic is most sensitive. Nevertheless, the coupling β 's for the modes

are still close enough to critical coupling from a power supply point of view.

VIII. CONCLUSION

The prototype of a harmonic kicker cavity as a 7.1 kW high-power device that deflects the electrons in/out of the CCR of the JLEIC was designed and fabricated. The cavity design was highly optimized for power loss, harmonic frequency tuning, and near-critical rf coupling. In particular, the rf coupling of all five harmonic modes was achieved by a single-loop coupler. As a high power device, the thermal load from rf heating was evaluated and the water cooling scheme that limited the overall temperature to around 70°C was designed using coupled multiphysics simulations. To compensate for the frequency deviations during the installation and operation, a tuning system consisting of five stubs that are inserted into the cavity was designed to have the tuning range of $\delta f/f \sim \pm 5.5 \times 10^{-4}$ for all the modes. The stub tuners are equipped with rf fingers that block the rf leakage, preventing excessive heating. rf breakdown in the Kilpatrick limit and multipacting were also investigated.

The cavity prototype was fabricated together with the multi-harmonic rf source (HAWG/HWAC) and controller, a tuning system, and a coupler set. Via a clamp-up bench test and trimming, the five harmonic frequencies are precisely tuned compensating the fabrication errors and other rf measurements showed the rf couplings and Q_0 's of the cavity are close to the nominal design values, making the cavity ready for the beam test.

ACKNOWLEDGMENTS

This material is based upon work supported by the U.S. Department of Energy, Office of Science, Office of Nuclear Physics under contract No. DE-AC05-06OR23177. Many people from the engineering group contributed to the fabrication of the cavity. Special thanks go to Jim Henry, Scott Williams, Gregory Grose, Roland Overton, Adam O'Brien, Jim Folkie, Vince Pope, and Danny Forehand.

APPENDIX A: PARAMETER FITTING OF ON-AXIS FIELD PROFILES IN THE QWR

The explicit expression for \mathcal{A}_n , σ_n , \mathcal{B}_n , ρ_n 's in terms of ξ , b are obtained from two-variable fitting of the field profiles from the CST-MWS simulations and listed in Table VIII. The field profiles were obtained by parameter scanning of b and ξ_0 , where $\xi_0 = \xi + 0.0133b = a/b + 0.0133b$ (the equation of threshold). The \mathcal{A}_n 's, σ_n 's, \mathcal{B}_n 's, ρ_n 's, and \mathcal{E}_n 's were extracted from the

TABLE VIII. The fitting from the CST-MWS simulation. The fitting equation = $A\xi^2 + B\xi + Cb^2 + Db + E$.

Modes	86.6 MHz	259.8 MHz	433 MHz	606.2 MHz	779.4 MHz
F_n					
A	0.1	-1.9	796.8	-119.7	8.5
B	-0.1	-1.5	832.7	-125.2	8.5
C	-0.6	-0.2	964.8	-146.9	8.5
D	-0.5	-0.6	1171	-180.4	10.4
E	0.0	-2.5	1538	-241.2	14.8
T_n					
A	-0.51	1.55	13.3	-2.46	-0.06
B	-0.13	0.38	1.15	-0.34	0.73
C	0.13	-0.3	1.17	1.44	0.97
D	0.31	-1.02	21.7	-5.06	1.99
E	0.76	-2.42	7.28	-3.42	2.95

postprocessing after a series of the CST-MWS simulations. The \mathcal{A}_n 's and \mathcal{B}_n 's are extracted as the peak values of the E_\perp and B_\perp , respectively. Then x value for $e^{-1/2}$ of the peak value would correspond to rms of the Gaussian, i.e., σ_n and ρ_n . The \mathcal{E}_n 's were directly evaluated from the shunt voltage V_\perp divided by g . How close the field profile $E_{\perp,n}$ is to the Gaussian mode was checked by obtaining integration of the field over the axis in the CST, which can be compared to $\sqrt{2\pi\sigma^2}\mathcal{A}_n$. Their ratios range 0.85–1, with a larger deviation tending to be with larger b . This implies the power calculation based on the Gaussian model can have errors up to 30%. Also \mathcal{A}_n was compared with \mathcal{E}_n with little differences. Here the ratio $\mathcal{A}_n/\mathcal{E}_n$ does not depend on ξ , b , only n .

The extracted data were fitted with a nonlinear regression equation $\chi(\xi, b) = A\xi^2 + B\xi + Cb^2 + Db + E$. In particular, the fringe field factor and transit time factor were fitted with the coefficients in Table VIII.

APPENDIX B: TAPERING AND TUNING MATRIX

The tapering and tuning matrix is obtained from the CST simulations. Based on the Slater perturbation theorem, the matrix elements are determined by a series of perturbative parameter scanning of h_j 's, tapering heights, and d_j 's, stub insertion depths while tracking the five harmonic modes. The tracking and fitting results are shown in Fig. 28 for tapering and Fig. 29 for tuning. The plots in Fig. 28, 29 are fitted to linear curves, whose slopes would constitute tapering matrix \mathcal{T}_t in (9) and tuner matrix \mathcal{T}_s in (10), respectively.

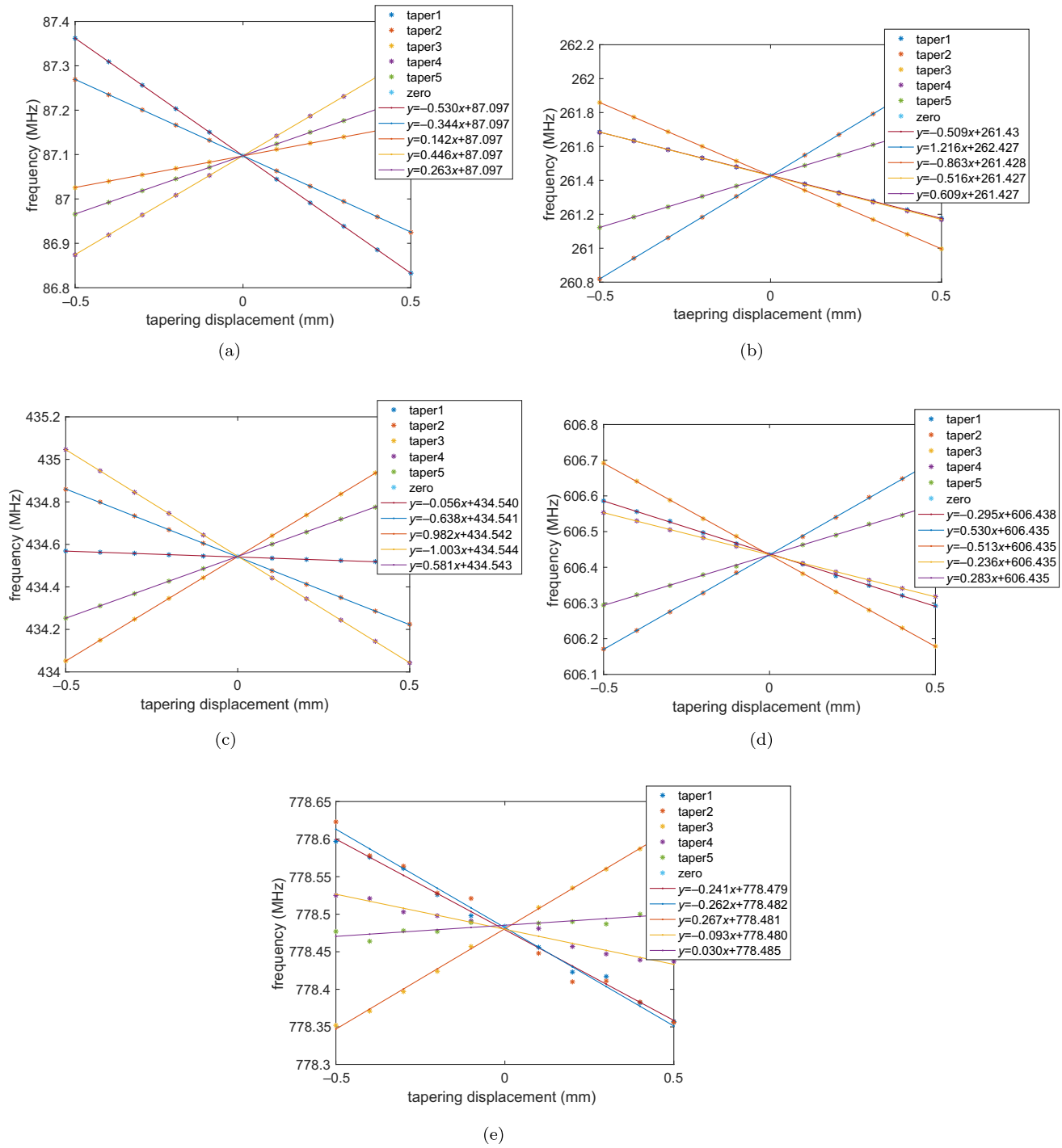


FIG. 28. The fitting for frequency tuning matrices of the tapering points. (a) The fitting for 86.6 MHz. (b) The fitting for 259.8 MHz. (c) The fitting for 433 MHz. (d) The fitting for 606.2 MHz. (e) The fitting for 779.4 MHz.

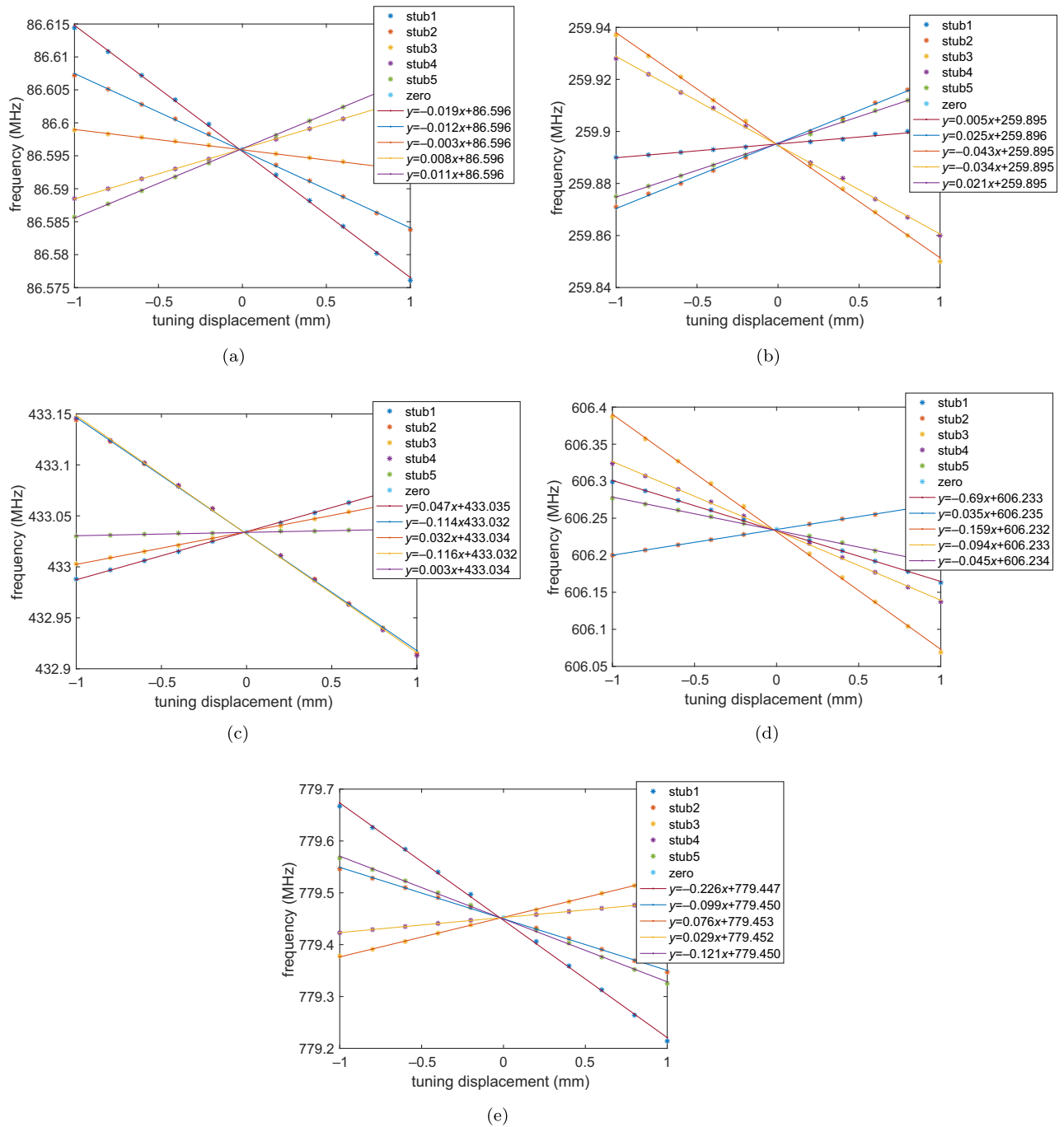


FIG. 29. The fitting for frequency tuning matrices of the stub insertion. (a) The fitting for 86.6 MHz. (b) The fitting for 259.8 MHz. (c) The fitting for 433 MHz. (d) The fitting for 606.2 MHz. (e) The fitting for 779.4 MHz.

TABLE IX. The fitting from the CST-MWS simulation for global frequency response.

Modes	86.6 MHz	259.8 MHz	433 MHz	606.2 MHz	779.4 MHz
The first stub					
\mathcal{A}	86.84		431.87	606.80	781.99
\mathcal{B}	0.24		-1.14	0.63	2.07
\mathcal{C}	0.08		0.04	0.10	0.10
\mathcal{A}'		0.045			
\mathcal{B}'		0.129			
\mathcal{C}'		-1.872			
\mathcal{D}'		0.000			
\mathcal{E}'		259.812			
The second stub					
\mathcal{A}	86.73	259.11	434.39	599.71	780.67
\mathcal{B}	0.13	-0.69	1.39	-6.48	0.75
\mathcal{C}	0.08	0.04	0.08	0.00	0.13
The third stub					
\mathcal{A}	86.62	260.29	431.75	607.97	778.11
\mathcal{B}	0.02	0.50	-1.26	1.80	-1.80
\mathcal{C}	0.13	0.08	0.02	0.08	0.04
The fourth stub					
\mathcal{A}	86.36	260.16	434.42	607.17	
\mathcal{B}	-0.24	0.37	1.42	1.00	
\mathcal{C}	0.03	0.09	0.08	0.09	
\mathcal{A}'					0.257
\mathcal{B}'					0.146
\mathcal{C}'					-2.267
\mathcal{D}'					-0.002
\mathcal{E}'					780.079
The fifth stub					
\mathcal{A}	86.36	259.16		606.57	781.04
\mathcal{B}	-0.24	-0.64		0.40	1.12
\mathcal{C}	0.04	0.03		0.11	0.10
\mathcal{A}'			-0.018		
\mathcal{B}'			0.279		
\mathcal{C}'			-4.900		
\mathcal{D}'			0.000		
\mathcal{E}'			433.011		

APPENDIX C: LONG RANGE TUNING

The frequency response to stub motion through a full travel distance of ± 15 mm is not linear as illustrated in Fig. 6(b), for example. Accordingly, frequency tuning based on a linear matrix (10) is not accurate away from the proximity of the default insertion. To predict an accurate tuning range over a full travel distance, the frequency response to each stub motion (with the other stubs held at the default position) is fitted to analytical nonlinear curves over a full travel distance (see Table IX):

$$f(x) = \mathcal{A} - \mathcal{B}e^{\mathcal{C}x}, \quad (\text{C1})$$

$$g(x) = \mathcal{A}' \cos(\mathcal{B}'x + \mathcal{C}') + \mathcal{D}'x^2 + \mathcal{E}'. \quad (\text{C2})$$

Here f , g are frequencies, x is displacement of each stub, and $\mathcal{A}, \mathcal{B}, \mathcal{C}, \mathcal{A}', \mathcal{B}', \mathcal{C}', \mathcal{D}', \mathcal{E}'$ are fitting constants. In “exceptional” cases, i.e., mode 2 with stub 1, mode 3 with stub 5, and mode 5 with stub 4, the curves are fitted by g in (C2), while the rest of cases are fitted by f in (C1). By the Slater cavity perturbation theorem, the frequency change is the sum of those by each stub motion. The frequency tuning is still based on an iteration of linear approximation (10) because it is difficult to solve a coupled system of nonlinear equations. The fitting by (C1), (C2) could make iteration processes shorter by using the tuning matrix that is displacement-dependent as

$$\mathcal{T}_{ij}(x) = \begin{cases} \text{if } (i, j) = (2, 1), (3, 5), (5, 4) \\ -\mathcal{A}'_{ij} \sin(\mathcal{B}'_{ij}x + \mathcal{C}'_{ij}) + 2\mathcal{D}'_{ij}x, \\ \text{otherwise} \\ -\mathcal{B}_i \mathcal{C}_{ij} e^{\mathcal{C}_{ij}x}. \end{cases} \quad (\text{C3})$$

The resulting tuning range is shown in Fig. 30(f) to be a little more limited than based on a linear response model. In Fig. 30(f), the stub travel distances “saturated” with frequency deviations in the range of $\delta f/f \sim 5.5 \times 10^{-4}$. In Fig. 6(b), one can see the curves are flatter near the cavity wall on the outer tube, reducing the frequency sensitivity.

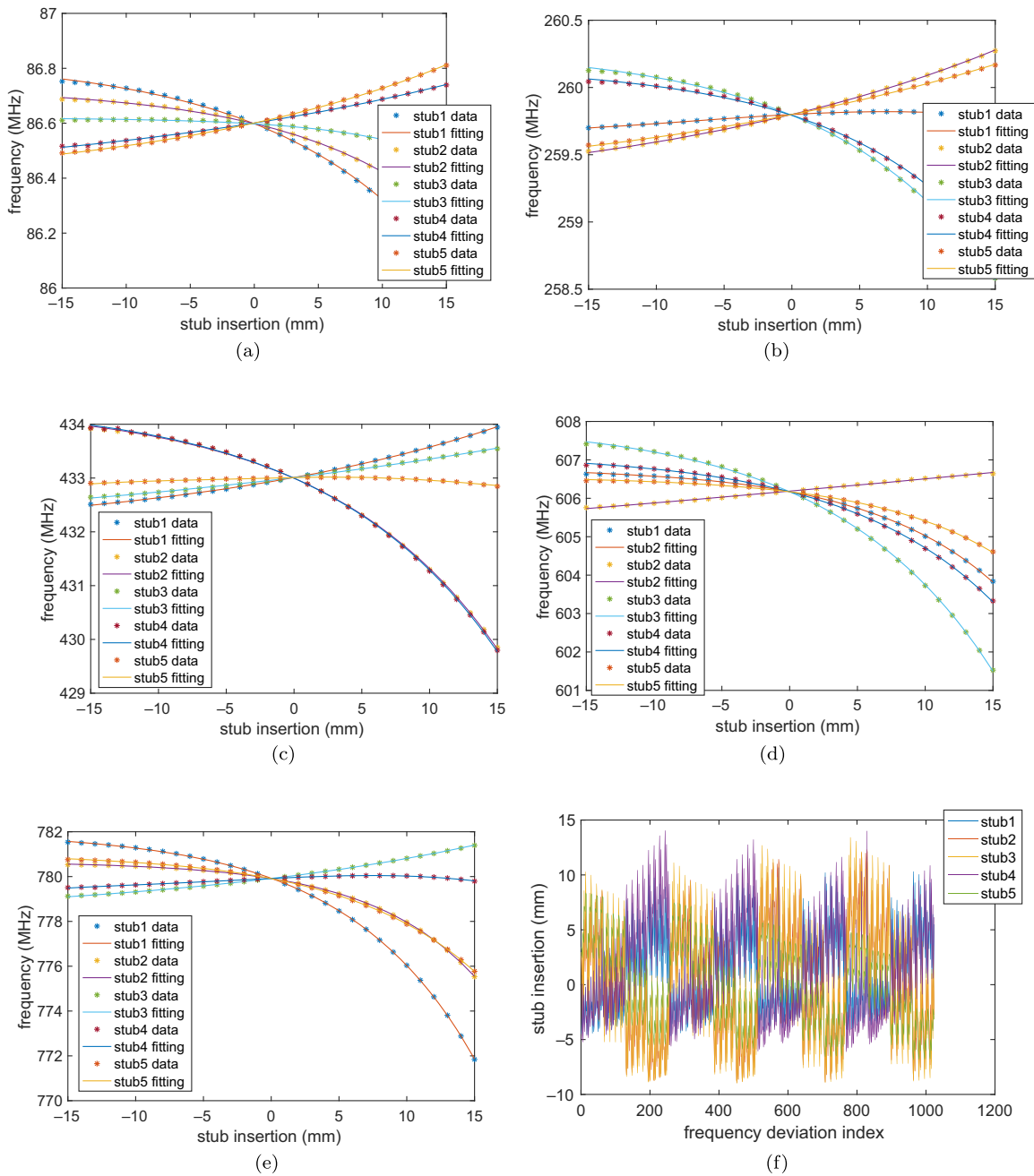


FIG. 30. The fitting for nonlinear frequency response over full insertion. (a) The fitting for 86.6 MHz. (b) The fitting for 259.8 MHz. (c) The fitting for 433 MHz. (d) The fitting for 606.2 MHz. (e) The fitting for 779.4 MHz. (f) The full tuning range based on nonlinear response.

[1] Y. Huang, H. Wang, R. A. Rimmer, S. Wang, and J. Guo, *Phys. Rev. Accel. Beams* **19**, 122001 (2016).
 [2] Y. Huang, H. Wang, R. A. Rimmer, S. Wang, and J. Guo, *Phys. Rev. Accel. Beams* **19**, 084201 (2016).
 [3] G. T. Park, J. Guo, R. A. Rimmer, H. Wang, and S. Wang, *Phys. Rev. Accel. Beams* **24**, 061002 (2021).

[4] J. Guo and H. Wang, Harmonic stripline kicker for MEIC bunched beam cooler, in *Proceedings of COOL2015, Newport News, VA, USA (JACoW, Geneva, 2015)*, TUPF10.
 [5] G. Park, J. Guo, S. Wang, R. Rimmer, and H. Wang, The beam dynamics of a fast harmonic kicker, JLAB Tech note, JLAB-TN-18-044.
 [6] G. Park, J. Guo, S. Wang, J. Henry, M. Marchlik, R. Rimmer, F. Marhauser, and H. Wang, Status update of a harmonic kicker development for JLEIC, in *Proceedings*

- of the 9th International Particle Accelerator Conference, Melbourne, Australia* (JACoW, Geneva, 2019), WEPRB099.
- [7] G. Park, J. Guo, S. Wang, F. Fors, R. Rimmer, and H. Wang, The development of a new fast harmonic kicker for the JLEIC circulator cooler ring, in *Proceedings of the 9th International Particle Accelerator Conference, Vancouver, Canada* (JACoW, Geneva, 2018), TUPAL068.
- [8] J. Guo *et al.*, (to be published).
- [9] Jefferson Lab Electron-Ion Collider Pre-Conceptual Design Report.
- [10] CST, simulation packages, <http://www.cst.com>.
- [11] A. Grudiev and W. Wuensch, A new local field quantity describing the high gradient limit of accelerating structures, in *Proceedings of LINAC08, Victoria, BC, Canada* (JACoW, Geneva, 2008), THP063.
- [12] S. Benedetti, A. Degiovanni, A. Grudiev, W. Wuensch, and U. Amaldi, RF design of a novel S-band backward traveling wave linac for proton therapy, in *Proceedings of LINAC2014, Geneva, Switzerland* (JACoW, Geneva, 2014), THPPP061.
- [13] D. Pritzkau, RF pulsed heating, SLAC National Accelerator Laboratory Report No. SLAC-R-577 UC-414.
- [14] H. Wang, Reconstruction of Cavity to Coupler Transition Field from 3D Eigensolutions (to be published).
- [15] The authors were notified that the CST installed a new solver, a lossy eigenmode solver, which can implement open boundary conditions and give accurate evaluations of external quality factors.
- [16] F. Marhauser, Calculations for RF cavities with dissipative materials, in *Proceedings of SRF2015, Whistler, BC, Canada* (JACoW, Geneva, 2015), THPB003.
- [17] W. K. H. Panofsky and W. A. Wenzel, *Rev. Sci. Instrum.* **27**, 967 (1956).
- [18] G. Park, J. Guo, S. Wang, R. Rimmer, F. Marhauser, and H. Wang, Beam impedance study on a harmonic kicker for the CCR of the JLEIC, in *Proceedings of the 63rd ICFA Advanced Beam Dynamics Workshop on Energy Recovery Linacs, Berlin, Germany* (JACoW, Geneva, 2019), WEP-NEC22.
- [19] Ansys Inc., <http://www.ansys.com>.
- [20] M. Marchlik *et al.*, JLAB Tech note, JLAB-TN-18-047 (to be published).
- [21] J. Guo, R. Rimmer, S. Williams, and M. Neubauer, Muon Inc. High Power Coaxial SRF Coupler Phase II Project Summary, JLAB Tech note, JLAB-TN-14-010.
- [22] S. Simrock, G. Petrosyan, A. Facco, V. Zviagintsev, and S. Andreoli, and R. Paparella, First demonstration of microphonic control of a superconducting cavity with a fast piezoelectric tuner, in *Proceedings of 2003 Particle Accelerator Conference, Portland, Oregon, USA* (JACoW, Geneva, 2003), ROAA004.
- [23] S. Ghosh, P. N. Patra, B. K. Sahu, A. Rai, G. K. Chaudhari, A. Pandey, D. Kanjilal, and A. Roy, Method to reduce microphonics in superconducting resonators, *Phys. Rev. ST Accel. Beams* **10**, 042002 (2007).
- [24] H. D. Schwarz, K. Fant, J. G. Judkins, M. Neubauer, and R. A. Rimmer, Development of a movable plunger tuner for the high-power RF cavity for the PEP-II B factory, in *Proceedings of the 1997 Particle Accelerator Conference, Vancouver, BC, Canada* (JACoW, Geneva, 1997).
- [25] S-bond Technology, <https://s-bond.com>.
- [26] E. O. Hammerstad and F. Bekkadal, A Microstrip Handbook, ELAB Report, STF 44 A74169, University of Trondheim, Norway (1975), pp. 98–110.
- [27] <https://www.microwaves101.com/encyclopedias/surface-roughness>.